THESIS

STOCHASTIC ANALYSIS AND PROBABILISTIC DOWNSCALING OF SOIL MOISTURE

Submitted by

Jordan P. Deshon

Department of Civil and Environmental Engineering

In partial fulfillment of the requirements

For the Degree of Master of Science

Colorado State University

Fort Collins, Colorado

Summer 2018

Master's Committee:

Advisor: Jeffrey D. Niemann

Timothy R. Green
Daniel S. Cooley

ABSTRACT

STOCHASTIC ANALYSIS AND PROBABILISTIC DOWNSCALING OF SOIL MOISTURE

Many applications require fine-resolution soil-moisture maps that exhibit realistic statistical properties (e.g., spatial variance and correlation). Existing downscaling models can estimate soil-moisture based on its dependence on topography, vegetation, and soil characteristics. However, observed soil-moisture patterns also contain stochastic variations around such estimates. The objectives of this research are to perform a geostatistical analysis of the stochastic variations in soil moisture and to develop downscaling models that reproduce the observed statistical features while including the dependence on topography, vegetation, and soil properties. Extensive soil-moisture observations from two catchments are used for the geostatistical analysis and model development, and two other catchments are used for model evaluation. The Equilibrium Moisture from Topography, Vegetation, and Soil (EMT+VS) model is used to downscale soil moisture, and the difference between the point measurements and the EMT+VS estimates are considered to be the stochastic variations. The stochastic variations contain a temporally stable pattern along with temporally unstable patterns. All of these patterns include spatially correlated and uncorrelated variations. Moreover, the spatial variance of the stochastic patterns increases with the mean moisture content. The EMT+VS model can reproduce the observed statistical features if it is generalized to include stochastic deviations from equilibrium soil moisture, variations in porosity, and measurement errors. It can also reproduce most observed properties if stochastic variations are inserted directly in its soil moisture outputs. These analyses and downscaling models provide insight into the nature of

stochastic variations in soil moisture and can be further tested by application to other catchments and larger regions.

ACKNOWLEDGMENTS

I gratefully acknowledge the United States Army Research Laboratory for its financial support through the Small Business Innovation Research program. I also thank Jeffrey Niemann, Timothy Green, Andrew Jones, and Daniel Cooley for their helpful suggestions and collaboration on this research.

TABLE OF CONTENTS

1. INTRODUCTION

Fine-resolution maps (10-30 m grid cells) of volumetric water content (soil moisture) are important for many applications. They can improve agricultural production (Holzman et al., 2014; Phillips et al., 2014), vector-borne infectious disease outbreak prediction (Montosi et al., 2012; Patz et al., 1998), weather and climate modeling (Pal and Eltahir, 2001; Seuffert et al., 2002), forest fire prediction (Bartsch et al., 2009), and crop yield quantification (de Wit and van Diepen, 2007; Green and Erskine, 2004).

For some applications, it is particularly important for the soil-moisture maps to reproduce the statistical properties of the observed patterns. For example, accurate assessment of spatial and temporal soil-moisture variability supports crop and water management (Chen et al., 2011). In addition, Wood (1997) demonstrated that proper characterization of soil moisture's spatial variability is important for accurate estimation of coarse-resolution evaporation during different atmospheric states (both low and high demands). Moreover, proper characterization of the soil-moisture probability density function (PDF) is useful for improving simulation of sub-grid processes in land-surface models, evaluating remotely sensed soil-moisture data, and estimating fine-scale hydrologic, ecological, and biogeochemical fluxes (Ryu and Famiglietti, 2005). Because soil moisture is a principle variable in determining soil strength (Horn and Fleige, 2003), reproducing observed ranges of soil moisture is also vital for assessing vehicle trafficability (Flores et al., 2014), vehicle impacts (Shoop et al., 2005), and soil damage (Vero et al., 2014).

Several studies have characterized the statistical properties of soil-moisture patterns including the PDF, spatial variability, and correlation structure. Various PDFs have been

evaluated by their ability to describe the observed spatial distribution of soil moisture. For large regions, a beta distribution (Ryu and Famiglietti, 2005) and a lognormal distribution (Choi and Jacobs, 2007) can fit the sample distributions well during dry conditions. However, these same studies concluded that a normal distribution fits the data better when considering the full range of conditions. For small catchments, a normal distribution has also been found to adequately describe the PDF of soil moisture (Western et al., 2002). In addition, the spatial variability of soil moisture has been demonstrated to change based on the spatial-average soil moisture (Famiglietti et al., 2008). Some studies have reported increasing spatial variability with increasing spatial average (De Lannoy et al., 2006; Famiglietti et al., 1998; Western and Grayson, 1998), while others have reported an inverse relationship (Brocca et al., 2007; Famiglietti et al., 1999; Hupet and Vanclooster, 2004). Still others observed maximum variability at intermediate values of the average (Owe et al., 1982; Vereecken et al., 2007). Also, the spatial correlation length of soil moisture varies between regions and can vary temporally within the same region. For example, studies have found increasing (Brocca et al., 2007), decreasing (Western et al., 1998), and site-dependent (Western et al., 2004) relationships between correlation length and spatial-average soil moisture.

Fine-resolution maps of soil moisture are typically produced by downscaling coarse-resolution data. Coarse-resolution soil moisture is available from various resources including Advanced Microwave Scanning Radiometer–EOS (AMSR-E) (Njoku et al., 2003), Soil Moisture and Ocean Salinity (SMOS) (Kerr et al., 2010), and Soil Moisture Active Passive (SMAP) (Entekhabi et al., 2010; Reichle et al., 2017). SMERGE is a synthesis of SMAP satellite-based data and model runs providing daily values from 1979 to 2015 (Crow et al., 2017). Geoinformation-based downscaling methods use a combination of fine-resolution topography,

vegetation, and soil data to infer fine-scale variations in soil moisture (Busch et al., 2012; Coleman and Niemann, 2013; Pellenq et al., 2003; Ranney et al., 2015). These methods rely on known relationships between soil moisture and topography (Grayson et al., 1997; Western et al., 1999), vegetation (Ranney et al., 2015), and soil characteristics (Famiglietti et al., 1998; Takagi and Lin, 2011). The soil moisture patterns generated by these methods reproduce the spatial structures implied by the site characteristics, but they have not been shown to reproduce the statistical properties of the observed soil moisture patterns.

Other downscaling methods specifically aim to reproduce soil moisture's statistical properties. For example, multifractal interpolation techniques have been proposed to downscale soil moisture (Kim and Barros, 2002; Kumar, 1999; Mascaro et al., 2010). While these methods are able to approximate the observed soil-moisture variability and correlation structure at multiple spatial scales, they downscale soil moisture to spatial resolutions (200-825 m) that may be too coarse for some applications. Additionally, they do not consider soil moisture's dependence on topography, vegetation, and soil characteristics.

The primary objectives of this research are: (1) to characterize the stochastic variability of soil moisture within the catchment scale and (2) to develop downscaling models that reproduce the observed statistical features of soil moisture (while including soil moisture's dependence on topography, vegetation, and soil characteristics). Extensive ground-based soil-moisture measurements from two catchments (Tarrawarra and Cache la Poudre) are used for the stochastic analysis and model development, and two other catchments (Nerrigundah and Satellite Station) are used for model evaluation. The Equilibrium Moisture from Topography, Vegetation, and Soil (EMT+VS) model (Ranney et al., 2015) is used to estimate soil moisture based on the available site properties (topography and vegetation). The deviations between the

observations and EMT+VS estimates are considered the stochastic variations. Geostatistical analysis is used to analyze these variations. Then, the EMT+VS model is generalized to simulate the stochastic variations. Two model versions are developed: the indirect model and the direct model. The indirect model introduces stochastic variability through the site properties that are supplied to the EMT+VS model. Because the variations are introduced through the inputs, the indirect model may be more transferable between catchments. The direct model introduces the stochastic variations directly in the soil moisture, which requires no assumptions about the factors causing the stochastic variability. The following section ("Resources") describes the study catchments and the existing EMT+VS model. Then, Section 3 ("Soil-Moisture Analysis") presents the methodology and results of the geostatistical analysis. Section 4 ("Model Development") shows the methodology and results for both generalized models. Finally, Section 5 ("Conclusions") summarizes the main conclusions from this study and discusses avenues for further research.

2. RESOURCES

2.1 Study Sites

Soil-moisture data are used from four catchments: Tarrawarra, Cache la Poudre, Nerrigundah, and Satellite Station. Tarrawarra and Cache la Poudre are used for model development because they have sampling locations that are dense enough to calculate reliable semivariograms for the geostatistical analysis. Additionally, both catchments have enough sample dates to observe how the semivariograms change in time and with mean moisture content. Nerrigundah and Satellite Station have fewer sampling locations and/or fewer observation dates, so they are used for model validation.

The Tarrawarra catchment (Western and Grayson, 1998) is in southern Victoria, Australia (37° 39’ S and 145° 26’ E) and has an approximate area of 10.5 ha. The vegetation consists of perennial improved pastures. The climate is sub-humid with a mean annual precipitation of 820 mm. Elevation data are available from a 5 m digital elevation model (DEM) (Figure 1a), and the maximum elevation difference (total relief) is approximately 25 m. Soil-moisture data are available on a 10 by 20 m grid at 454 locations. These data were collected using a time-domain reflectometer (TDR) in the top 30 cm of the soil (Western et al., 1999). Samples were taken on 13 dates from September 27, 1995 to November 29, 1996.

The Cache la Poudre catchment (Lehman and Niemann, 2008) is near Rustic, Colorado, USA (40° 41’ 56” N and 105° 30’ 30” W) and has an approximate area of 8.0 ha. The climate is semiarid with a mean annual precipitation of 400 mm. Elevation data are available from a 15 m DEM (Figure 1b), and the total relief is approximately 118 m. The catchment has aspect dependent vegetation with coniferous forest on the north-facing hillslope and shrubs on the

south-facing hillslope. Fractional vegetation cover data (generated from litter depth measurements and vertical photographs) are available on the 15 m grid. Soil-moisture data are also available on the 15 m grid at 350 locations. These data were collected using a TDR in the top 5 cm of the soil. Samples were taken on nine dates from April 22, 2008 to June 24, 2008.

The Nerrigundah catchment (Walker et al., 2001) is near Dungog, New South Wales, Australia (32° 19' S and 151° 43' E) and has an approximate area of 6.0 ha. The vegetation consists of natural grasses. The climate is sub-humid with a mean annual precipitation of 1,000 mm. Topographic data are available from a 20 m DEM (Figure 1c), and the total relief is approximately 38 m. Soil-moisture data are available on the same 20 m grid at 238 locations. These data were collected using a TDR in the top 15 cm of the soil (Walker et al., 2001). Samples were taken on 12 dates from August 27, 1997 to September 22, 1997.

The Satellite Station catchment (Western et al., 2004) is approximately 70 km north of Auckland, New Zealand (36° 24' S and 174° 42' E) and has an approximate area of 60 ha. The vegetation is predominately pasture. The climate is sub-humid with a mean annual precipitation of 1,200 mm. Topographic data are available from a 40 m DEM (Figure 1d), and the total relief is approximately 80 m. Soil-moisture data are available on the 40 m grid at 370 locations. These data were collected using a TDR in the top 30 cm of the soil (Western et al., 2004). Samples were taken on six dates from March 25, 1998 to October 30, 1999.

2.2 Existing EMT+VS Model

The EMT+VS model uses an analytical expression to calculate fine-resolution soil-moisture patterns from temporally varying spatial-average soil moisture values. The fine-resolution variations in soil moisture are inferred from fine-resolution topographic data and fine-resolution vegetation and soil data if available. A detailed description of the EMT+VS model is

presented by Coleman and Niemann (2013) and Ranney et al. (2015), so only a brief summary is provided here.

The EMT+VS model is based on the water balance for a soil layer whose upper limit is at the ground surface. Four processes can add or remove water from this layer: infiltration F, deep drainage G, lateral flow L, and evapotranspiration E (ET). Assuming equilibrium at each time, the water balance can be written:

$$\int_A F dA = \int_A G dA + L + \int_A E dA \tag{1}$$

where A is the land area that is upslope from the edge of a fine-resolution grid cell.

Infiltration is described using a simple approach that accounts for interception by vegetation:

$$F = F_0 \left(1 - \lambda V\right) \tag{2}$$

where F_0 is the infiltration rate where the canopy is absent, λ is the interception efficiency of the vegetation, and V is the fractional vegetation cover. The infiltration model can also account for orographic precipitation and elevation dependent potential ET (Cowley et al., 2017), but those components are neglected here due to the small elevation ranges at the application catchments.

Deep drainage is described using Darcy's Law under the assumption that gravity controls the hydraulic gradient and using the Campbell (1974) equation to estimate the unsaturated hydraulic conductivity. Specifically:

$$G = K_{s,v} \left(\frac{\theta}{\phi} \right)^{\gamma_v} \tag{3}$$

where $K_{s,v}$ is vertical saturated hydraulic conductivity, θ is the depth-averaged volumetric soil moisture in the soil layer, ϕ is porosity, and γ_v is the vertical pore disconnectedness index.

Lateral flow is also described using Darcy's Law under the assumption that the lateral hydraulic gradient is a function of the topographic slope, which is similar to TopModel (Beven and Kirkby, 1979). The thickness of the soil layer is modeled as a function of topographic curvature (Heimsath et al., 1999). Thus, lateral flow is:

$$L = \delta_0 \left(\frac{\kappa_{\min} - \kappa}{\kappa_{\min}} \right) c\iota K_{s,v} \left(\frac{\theta}{\phi} \right)^{\gamma_h} S^{\varepsilon} \tag{4}$$

where δ_0 is the layer thickness where topographic curvature is zero, $\kappa_{\min}$ is the minimum topographic curvature where the layer is present, κ is topographic curvature, c is the length of the fine-resolution grid cell, ι is the anisotropy of the saturated hydraulic conductivity, γ_h is the horizontal pore disconnectedness index, S is topographic slope, and ε is a parameter relating the horizontal hydraulic gradient to topographic slope.

The ET expression begins with a supplied spatial-average potential ET. The potential ET is partitioned into a potential evaporation and a potential transpiration using the fractional vegetation cover V. It is also partitioned into radiation and aerodynamic terms using the Priestley-Taylor assumption (Priestley and Taylor, 1972). Spatial variations in solar insolation are included in the radiation terms using the Potential Solar Radiation Index (PRSI), which depends on the topographic slope and aspect among other variables (Dingman, 2002). The ET expression is:

$$E = E_p \left[\eta V + (1 - V)^{\mu} \right] \left[\frac{I_p}{1 + \alpha} \left(\frac{\theta}{\phi} \right)^{\beta_r} + \frac{\alpha}{1 + \alpha} \left(\frac{\theta}{\phi} \right)^{\beta_a} \right] \tag{5}$$

where E_p is the potential ET, I_p is the PSRI, η is the portion of transpiration that is derived from the soil layer, μ is the shading effect on soil evaporation, α is the Priestly-Taylor coefficient minus one, β_r is the radiation ET exponent, and β_a is the aerodynamic ET exponent.

The soil moisture is determined from the water balance using a solution strategy from Coleman and Niemann (2013). First, a set of analytical solutions is obtained for soil moisture under the assumption that each of the outflow terms in the water balance dominates. Then, the final soil-moisture estimate is determined by a weighted average of the analytical solutions, where the weights are the magnitudes of the outflow terms in the water balance. The final soil-moisture estimate θ is:

$$\theta = \frac{w_G\theta_G + w_L\theta_L + w_R\theta_R + w_A\theta_A}{w_G + w_L + w_R + w_A} \tag{6}$$

where θ_G, θ_L, θ_R, and θ_A are the analytical soil-moisture values if deep drainage, lateral flow, radiation ET, and aerodynamic ET dominate, respectively. The variables w_G, w_L, w_R, and w_A are the associated weights.

The analytical soil moisture values are:

$$\theta_G = \bar{\theta}\frac{\mathrm{DDI}}{\overline{\mathrm{DDI}}} \tag{7}$$

$$\theta_L = \bar{\theta}\frac{\mathrm{LFI}}{\overline{\mathrm{LFI}}} \tag{8}$$

$$\theta_R = \bar{\theta}\frac{\mathrm{REI}}{\overline{\mathrm{REI}}} \tag{9}$$

$$\theta_A = \bar{\theta}\frac{\mathrm{AEI}}{\overline{\mathrm{AEI}}} \tag{10}$$

where $\bar{\theta}$ is the spatial-average soil moisture, DDI is the deep drainage index, LFI is the lateral flow index, REI is the radiation ET index, and AEI is the aerodynamic ET index. The variables $\overline{\text{DDI}}$, $\overline{\text{LFI}}$, $\overline{\text{REI}}$, and $\overline{\text{AEI}}$ are the spatial-averages of the indices. The indices are:

$$\text{DDI} = \phi\left(\frac{1-\lambda V}{K_{s,v}}\right)^{1/\gamma_v} \tag{11}$$

$$\text{LFI} = \phi\left(\frac{1-\lambda V}{\delta_0 \iota K_{s,\text{v}}}\right)^{1/\gamma_h}\left(\frac{A}{cS^{\varepsilon}}\right)^{1/\gamma_h}\left(\frac{\kappa_{\min}}{\kappa_{\min}-\kappa}\right)^{1/\gamma_h} \tag{12}$$

$$\text{REI} = \phi\left(\frac{1+\alpha}{E_p}\right)^{1/\beta_r}\left(\frac{1}{I_p}\right)^{1/\beta_r}\left[\frac{1-\lambda V}{\eta V+(1-V)^{\mu}}\right]^{1/\beta_r} \tag{13}$$

$$\text{AEI} = \phi\left(\frac{1+\alpha}{E_p\alpha}\right)^{1/\beta_a}\left[\frac{1-\lambda V}{\eta V+(1-V)^{\mu}}\right]^{1/\beta_a} \tag{14}$$

Spatial variations in DDI are produced by spatial variations in V and soil properties if fine-resolution data are available to describe soil variations. Spatial variations in LFI are produced by variations in κ, A, and S (and potentially vegetation and soil properties). Spatial variations in REI are produced by variations in I_p (and possibly vegetation and soil variations). Spatial variations in AEI are produced by vegetation and soil variations if fine-resolution data are available. The weights are:

$$w_G = \left(\frac{\bar{\theta}}{\overline{\text{DDI}}}\right)^{\gamma_v} \tag{15}$$

$$w_L = \left(\frac{\bar{\theta}}{\overline{\text{LFI}}}\right)^{\gamma_h} \tag{16}$$

$$w_R = \left(\frac{\bar{\theta}}{\overline{\text{REI}}}\right)^{\beta_r} \tag{17}$$

$$w_A = \left(\frac{\bar{\theta}}{\overline{\mathrm{AEI}}} \right)^{\beta_a} \tag{18}$$

The weights vary in time due to temporal variations in $\bar{\theta}$.

For the present study, fine-resolution topographic and vegetation data are used as inputs at Cache la Poudre, while only topographic data are used at the other catchments (it is assumed that $V = 1.0$ for these other catchments). Fine-resolutions soil data was not included because Ranney et al. (2015) found that soil properties were not useful when downscaling. The spatial-average soil moisture $\bar{\theta}$ is calculated from the available soil-moisture observations on each date. The remaining parameter values (Table 1) are obtained from the calibrations performed by Hoehn (2016) and Hoehn et al. (2017). In those calibrations, the allowable parameter ranges were determined from the available catchment information. Within those ranges, the parameter values were chosen to maximize the average Nash Sutcliffe Coefficient of Efficiency from all available dates.

3. SOIL-MOISTURE ANALYSIS

3.1 Analysis Methodology

The soil-moisture observations from the study catchments are assumed to be the sum of a deterministic and a stochastic component. The deterministic component contains the variations caused by soil moisture's dependence on topography and other fine-resolution variables and can be estimated using the pre-existing EMT+VS model. The stochastic component represents variations around the deterministic component. Thus, the observed stochastic component π_{obs} can be estimated as:

$$\pi_{obs} = \theta_{obs} - \theta \tag{19}$$

where θ_{obs} is the observed soil-moisture pattern and θ is the EMT+VS model's estimated pattern.

The π_{obs} patterns can also be decomposed into temporally stable and unstable patterns. The stable pattern is a time-invariant stochastic pattern that contributes to π_{obs} to some extent on every sample date. The stable stochastic pattern $\pi_{s,obs}$ can be estimated as the temporal average of the observed stochastic patterns:

$$\pi_{s,obs} = \mathrm{E}\left[\pi_{obs}\right] \tag{20}$$

where $\mathrm{E}[\ ]$ denotes the temporal average. The unstable stochastic patterns $\pi_{u,obs}$ are variations around the stable pattern on each date and can be estimated as:

$$\pi_{u,obs} = \pi_{obs} - \pi_{s,obs} \tag{21}$$

The patterns for θ_{obs}, π_{obs}, $\pi_{s,obs}$, and $\pi_{u,obs}$ are analyzed using semivariograms. This technique was introduced by Matheron (1963) and has been previously applied to θ_{obs} patterns (De Lannoy et al., 2006; Korres et al., 2015; Petrone et al., 2004; Western et al., 1998; Western et al., 2004). However, it has not been used to examine π_{obs}, $\pi_{s,obs}$, or $\pi_{u,obs}$. The sample semivariogram g_s is calculated using:

$$g_s(h) = \frac{1}{2N(h)} \sum_{i,j} \left(z_i - z_j \right)^2 \tag{22}$$

where h is a lag or separation distance between two selected points in a catchment, N is the number of pairs of points for each lag, i and j are indices for the two locations separated by distance h, and z_i and z_j are the values of the variable of interest at those two locations (i.e. θ_{obs}, π_{obs}, $\pi_{s,obs}$, or $\pi_{u,obs}$ in the analyses below). The number of lag bins was determined as the number of fine-resolution grid cells in the shorter of the two spatial dimensions. These bins were divided into equal sizes based on the maximum possible distance between two points.

The semivariogram has three main properties: the nugget, range, and sill. The nugget is the y-intercept of a semivariogram, the range is the lag beyond which the semivariance becomes relatively constant, and the sill is the value of that relatively constant semivariance. The nugget is produced by spatially uncorrelated variability and can be caused by measurement error and sub-grid variability (Western et al., 2004). The difference between the sill and the nugget (the partial sill) describes the contribution of spatially correlated variability. The range is related to the correlation length.

An exponential semivariogram model with a nugget was fit to the sample semivariogram of each pattern using a weighted least squares method from Cressie (1985). The exponential

form was selected because it usually fits the sample semivariograms well (McBratney and Webster, 1986; Western et al., 2004) compared with other models (e.g, spherical, circular, etc.). The exponential semivariogram g_e has the form:

$$g_e(h) = \sigma_n^2 + \sigma_s^2\left(1 - \mathrm{e}^{-h/r}\right) \tag{23}$$

where σ_n^2 is the nugget, σ_s^2 is the partial sill, r is the correlation length, and the sill is equal to $\sigma_n^2 + \sigma_s^2$. Thus, the nugget, partial sill, and correlation length of the sample semivariograms can be estimated by σ_n^2, σ_s^2, and r, respectively.

3.2 Analysis Results

The temporal-average semivariograms of θ_{obs} and π_{obs} are shown as symbols in Figure 2 (all figures in this section also show modeling results, but those results are discussed later). The θ_{obs} semivariogram exhibits both a nonzero nugget and partial sill at both catchments. The sill at Tarrawarra is larger than Cache la Poudre, and the contributions of nugget and partial sill are different. The nugget comprises a much smaller portion of the sill at Tarrawarra (13%) than at Cache la Poudre (55%), which suggests that correlated variability plays a much larger role in θ_{obs} at Tarrawarra than at Cache la Poudre. The correlation lengths are similar at both catchments (about 30 m at Tarrawarra and about 40 m at Cache la Poudre). Western et al. (1998) used visual inspection to estimate the semivariogram properties for θ_{obs} at Tarrawarra. They estimated that the nugget comprises 29% of the sill and found an average correlation length of 50 m.

The contribution of the stochastic component to the overall soil-moisture observations can be examined by comparing the sills of π_{obs} and θ_{obs}. The sill for π_{obs} is approximately

64% of the sill for θ_{obs} at Tarrawarra and about 84% at Cache la Poudre. Thus, the stochastic variations are important at both catchments, but more so at Cache la Poudre. The sill of Cache la Poudre is slightly larger than Tarrawarra. At Tarrawarra, the nugget for π_{obs} is 47% of the sill, and the correlation length is approximately 34 m. At Cache la Poudre, the nugget is 56% of the sill, and the average correlation length is approximately 21 m. Thus, both catchments have roughly equal contributions from correlated variability to π_{obs}, but Cache la Poudre has a slightly larger contribution of uncorrelated variability. At Tarrawarra, the correlation lengths of π_{obs} from individual dates range from 19 to 135 m (compared to 18 to 65 m for θ_{obs}), while at Cache la Poudre it ranges from 9 to 31 m (compared to 10 to 71 m for θ_{obs}). The correlation lengths of the pre-existing EMT+VS model θ range from 28 to 96 m at Tarrawarra and from 32 to 71 m at Cache la Poudre.

The diamonds in Figure 3 show the semivariogram of $\pi_{s,obs}$. The sill for $\pi_{s,obs}$ is a substantial portion of the sill for π_{obs} at both catchments (30% at Tarrawarra and 41% at Cache la Poudre). The higher percentage at Cache la Poudre suggests that the stable stochastic pattern plays a larger role at this catchment. At Tarrawarra, the nugget for $\pi_{s,obs}$ is 14% of the sill, and the correlation length is approximately 31 m. At Cache la Poudre, the nugget for $\pi_{s,obs}$ is 48% of the sill, and the correlation length is approximately 25 m. Thus, uncorrelated variability plays a larger relative role in $\pi_{s,obs}$ for Cache la Poudre than Tarrawarra.

The triangles in Figure 3 show the temporal-average semivariogram of $\pi_{u,obs}$. At Tarrawarra, the nugget for $\pi_{u,obs}$ is 62% of the sill, and the correlation length is approximately

45 m. At Cache la Poudre, the nugget for $\pi_{u,obs}$ is 48% of the sill, and the correlation length is approximately 14 m. Thus, in contrast to the stable patterns, uncorrelated variation plays a smaller relative role in $\pi_{u,obs}$ for Cache la Poudre than Tarrawarra.

Figure 4 plots the semivariogram properties of π_{obs} on each date against the associated spatial-average soil moisture $\bar{\theta}$. The nugget remains relatively constant at Tarrawarra, but it increases with $\bar{\theta}$ at Cache la Poudre. The correlation length of π_{obs} exhibits no dependence on $\bar{\theta}$ at either catchment. Western et al. (2004) found that the correlation length of soil moisture θ_{obs} increases with $\bar{\theta}$ at multiple catchments. The present results then suggest that this increasing trend is due to the deterministic component rather than the stochastic component. The partial sill for π_{obs} increases with $\bar{\theta}$ at Tarrawarra, which indicates a greater contribution from correlated variation on wetter dates. However, the partial sill remains fairly constant at Cache la Poudre. Western et al. (2004) reported that the variance of θ_{obs} increases with $\bar{\theta}$ at multiple catchments. Similar behavior is implied by the nuggets and partial sills of π_{obs} at both catchments. However, the increasing variance is due to increasing correlated variation at Tarrawarra and increasing uncorrelated variation at Cache la Poudre.

Figure 5 plots the semivariogram properties of $\pi_{u,obs}$ on each date against the associated $\bar{\theta}$. The nugget exhibits no dependence on $\bar{\theta}$ at either catchment, indicating that the uncorrelated variance in $\pi_{u,obs}$ remains fairly constant. Similarly, the correlation lengths exhibit no clear relationship with $\bar{\theta}$ at either catchment. For two dates at Tarrawarra, the exponential semivariogram fits the sample semivariogram poorly. To accommodate for this anomaly, the 7

largest lags (of the 23 total) were excluded when fitting the exponential semivariogram. This modification produced more reasonable semivariogram properties for one date, but an unusually large correlation length (197 m) was still estimated for the other date (this value falls beyond the limits of the graph in Figure 5). The partial sill increases with $\bar{\theta}$ at both catchments, which indicates a greater contribution from correlated variance during wetter conditions. Overall, these results suggest that the behavior of the unstable stochastic patterns is similar at both catchments.

The differences between the semivariogram properties in Figure 4 and Figure 5 reveal the influence of $\pi_{s,obs}$ on the stochastic patterns. At Cache la Poudre, for example, subtracting $\pi_{s,obs}$ from π_{obs} results in a larger nugget in $\pi_{u,obs}$ (compared to π_{obs}) for dry conditions. In contrast, this subtraction tends to decrease the nugget in $\pi_{u,obs}$ for wet conditions. Although the stable pattern is constant, this example demonstrates how its combination with the unstable patterns decreases the nugget of π_{obs} on drier dates and increases the nugget on wetter dates. Thus, at Cache la Poudre, the nugget of π_{obs} has a positive relationship with $\bar{\theta}$, while the nugget of $\pi_{u,obs}$ remains relatively constant.

4. MODEL DEVELOPMENT

4.1 Indirect Model Methodology

The indirect generalization of the EMT+VS model introduces stochastic variations by treating some model inputs as random variables. Although many inputs might contain spatial variations, the goal is to reproduce the observed stochastic features using as few random variables as possible. Thus, stochastic variations are included in only three ways: porosity, soil moisture disequilibrium, and measurement error.

Porosity has been shown to vary substantially at the catchment scale (Bakr et al., 1978). A stochastic porosity ϕ^* is included in the model by combining the existing calibrated porosity value ϕ with a stochastic perturbation p^*:

$$\phi^* = \phi\left(1 + p^*\right) \tag{24}$$

Because porosity is temporally constant under most conditions (except after soil disturbances, such as tillage), p^* is considered a stable stochastic pattern. Thus, only a single pattern is generated and used on each sample date. Studies have also demonstrated that porosity can have both spatial correlation (Bakr, 1976; Wang and Shao, 2013) and sub-grid variability (Duffera et al., 2007). Thus, p^* is constructed using a correlated random field p_c^* and an uncorrelated random field p_u^*:

$$p^* = p_c^* + p_u^* \tag{25}$$

Both p_c^* and p_u^* are assumed to be normally distributed with zero mean and homogeneous. Heteroscedasticity of the π_{obs}, $\pi_{s,obs}$, and $\pi_{u,obs}$ patterns was explored, but no consistent

behavior was observed for the two catchments (see APPENDIX). p_c^* is assumed to have a separable exponential correlation function and is generated using Fast Sequential Simulation (Dolloff and Doucette, 2014). Generating fields of p_c^* requires specification of its standard deviation σ_{p_c} and correlation length ρ_p. Similarly, generating fields of p_u^* requires specification of its standard deviation σ_{p_u}.

The pre-existing EMT+VS model calculates soil moisture by assuming equilibrium between the inflows and outflows of the soil layer. In reality, these flows are usually unbalanced and soil moisture is dynamic (e.g., Gaur and Mohanty, 2016). To allow deviations from equilibrium, the indirect model includes a stochastic variable. Specifically, when the equilibrium condition is imposed, the equilibrium soil moisture is considered stochastic (θ^*) and assumed to be:

$$\theta^* = \theta\left(1 + d^*\right) \tag{26}$$

where d^* is a random field that characterizes the deviations from equilibrium. Because such deviations vary in time, d^* is considered an unstable stochastic variable, so different patterns are generated for each date. To maintain parsimony, d^* is assumed to contain only a correlated pattern. Similar to porosity, d^* is assumed to be normally distributed with zero mean and homogeneous. Thus, generating fields of d^* requires specification of its standard deviation σ_d and correlation length ρ_d.

Including the porosity perturbation p^* and the deviation from equilibrium d^* in the EMT+VS model development produces new stochastic indices DDI^*, LFI^*, REI^*, and AEI^*:

$$\mathrm{DDI}^{*}=\frac{\phi\left(1+p^{*}\right)}{1+d^{*}}\left[\frac{\left(1-\lambda V\right)}{K_{s,v}}\right]^{1/\gamma_v} \tag{27}$$

$$\mathrm{LFI}^{*}=\frac{\phi\left(1+p^{*}\right)}{1+d^{*}}\left[\frac{\left(1-\lambda V\right)}{\delta_0 \iota K_{s,\mathrm{v}}}\right]^{1/\gamma_h}\left(\frac{A}{cS^{\varepsilon}}\right)^{1/\gamma_h}\left(\frac{\kappa_{\min}}{\kappa_{\min}-\kappa}\right)^{1/\gamma_h} \tag{28}$$

$$\mathrm{REI}^{*}=\frac{\phi\left(1+p^{*}\right)}{1+d^{*}}\left(\frac{1+\alpha}{E_p}\right)^{1/\beta_r}\left(\frac{1}{I_p}\right)^{1/\beta_r}\left[\frac{\left(1-\lambda V\right)}{\eta V+(1-V)^{\mu}}\right]^{1/\beta_r} \tag{29}$$

$$\mathrm{AEI}^{*}=\frac{\phi\left(1+p^{*}\right)}{1+d^{*}}\left(\frac{1+\alpha}{E_p\alpha}\right)^{1/\beta_a}\left[\frac{\left(1-\lambda V\right)}{\eta V+(1-V)^{\mu}}\right]^{1/\beta_a} \tag{30}$$

These stochastic indices are then used to calculate new stochastic soil moisture values using Equations 7-10 (θ_G^{*}, θ_L^{*}, θ_R^{*}, and θ_A^{*}). New stochastic weights are calculated using Equations 15-18 (w_G^{*}, w_L^{*}, w_R^{*}, and w_A^{*}).

In addition to the natural stochastic variations, the soil moisture observations also include measurement errors (Coleman and Niemann, 2013; Western and Grayson, 1998). Measurement errors must be simulated in order for the model to reproduce the properties of the observed soil moisture patterns. Measurement errors e^{*} are included by revising Equation 6 to become:

$$\theta^{*}=\frac{w_G^{*}\theta_G^{*}+w_L^{*}\theta_L^{*}+w_R^{*}\theta_R^{*}+w_A^{*}\theta_A^{*}}{w_G^{*}+w_L^{*}+w_R^{*}+w_A^{*}}+e^{*} \tag{31}$$

TDR measurement errors do not depend on spatial-average soil moisture (Roth et al., 1990), so Equation 31 assumes that the measurement errors are additive. The pattern of measurement error differs on each sampling date, so e^{*} is considered temporally unstable and different patterns are generated for each date. Measurement error is also expected to be independent between sampling locations, so e^{*} is considered an uncorrelated random field. Thus, generating fields of e^{*} field requires only specification of its standard deviation σ_e.

In the end, the indirect model introduces six new time-invariant parameters (σ_{p_c}, ρ_p, σ_{p_u}, σ_d, ρ_d, and σ_e) that must be estimated before soil-moisture simulations can be generated. For Tarrawarra and Cache la Poudre, these parameters estimated using the graphs shown in Figure 4 and Figure 5. To generate these figures, the indirect model's stochastic component π^*, stable pattern π_s^*, and the unstable patterns π_u^* are determined based on the same procedure from the analysis methodology:

$$\pi^* = \theta^* - \theta \tag{32}$$

$$\pi_s^* = E\left[\pi^*\right] \tag{33}$$

$$\pi_u^* = \pi^* - \pi_s^* \tag{34}$$

To ensure the stability of results, 2,000 model realizations were generated for each date, and the average semivariogram was used, though useful results can also be generated using fewer realizations (e.g., 500 realizations). The parameters were manually calibrated to minimize the root-mean-squared error (RMSE) between the observed and modeled semivariogram properties. Specifically, the parameters associated with unstable patterns (σ_d, ρ_d, and σ_e) were first adjusted to minimize RMSE between $\pi_{u,obs}$ and π_u^*. Then, the parameters associated with stable patterns (σ_{p_c}, ρ_p, and σ_{p_u}) were adjusted to minimize RMSE between π_{obs} and π^*. The calibrated parameters for the indirect model are shown in Table 2.

The indirect model also allows calculation of confidence limits for the EMT+VS model's estimated soil moisture (θ). For each fine-resolution grid cell, all 2,000 realizations of π^* were sorted from smallest to largest, and the empirical cumulative distribution function (CDF) was

computed using the plotting position formula from Cunnane (1978). The desired quantiles are computed by linearly interpolating between the CDF values that are represented in the dataset.

4.2 Direct Model Methodology

The direct model introduces stochastic variations directly in the final EMT+VS soil moisture. This model only introduces unstable stochastic patterns, so it is applicable if soil-moisture downscaling is only required for a single date. The direct model soil moisture θ_d^* is:

$$\theta_d^* = \theta\left(1 + a^* + b^*\right) + c^* \tag{35}$$

where θ is the pre-existing EMT+VS estimate, a^* is a correlated random field with a separable exponential correlation function, b^* is an uncorrelated random field, and c^* is an uncorrelated random field (representing measurement error). a^*, b^*, and c^* are assumed to be normally distributed with zero means and spatially homogeneous. Generating fields of a^* requires specification of its standard deviation σ_a and correlation length ρ_a. Generating fields of b^* requires specification of its standard deviation σ_b, and generating fields of c^* requires specification of its standard deviation σ_c.

In the end, the direct model introduces four new parameters (σ_a, ρ_a , σ_b, and σ_c) that must be estimated before soil-moisture simulations can be generated. Because this model does not introduce stable stochastic variations, these parameters estimated using only the graphs shown in Figure 4. The direct models' stochastic component π_d^*, stable pattern $\pi_{s,d}^*$, and its unstable patterns $\pi_{u,d}^*$ can be estimated as:

$$\pi_d^* = \theta_d^* - \theta \tag{36}$$

$$\pi_{s,d}^* = E\left[\pi_d^*\right] \tag{37}$$

$$\pi^*_{u,d} = \pi^*_d - \pi^*_{s,d} \tag{38}$$

Again, 2,000 model realizations were generated for each date, and the average semivariogram of all realizations was used. The direct model parameters were manually calibrated to minimize the RMSE between the semivariogram properties of π^*_d and π_{obs} using Figure 4. The calibrated parameters for the direct model are shown in Table 3.

The direct model allows confidence limits for θ to be computed analytically. Because direct model's stochastic variation is produced by a linear combination of normally distributed random variables, the distribution of π^*_d is also normal (Johnson and Wichern, 2002). Therefore, the standard deviation of the direct model's stochastic component $\sigma_{\pi^*_d}$ can be determined from the following equation:

$$\sigma_{\pi^*_d} = \sqrt{\left(\theta\sqrt{\sigma_a^2 + \sigma_b^2}\right)^2 + \sigma_c^2} \tag{39}$$

This standard deviation is then combined with the z-scores to calculate the desired quantiles (Isotalo, 2001).

4.3 Calibrated Model Results

The temporal-average semivariograms for the modeled soil moisture (θ^* and θ^*_d) and the associated stochastic components (π^* and π^*_d) are shown in Figure 2. For both soil moisture and its stochastic component, the models reproduce the observed nugget, correlation length, and partial sill at both catchments. Reproducing the nugget and partial sill indicates that the models include the correct amounts of uncorrelated and correlated variations, respectively. The reproduction of the correlation length suggests that the models include the appropriate correlation lengths in their correlated patterns.

The semivariograms for the modeled stable patterns (π_s^* and $\pi_{s,d}^*$) and the temporal-average semivariograms for the modeled unstable patterns (π_u^* and $\pi_{u,d}^*$) are shown in Figure 3. The indirect model closely approximates the contribution of the stable pattern to the overall stochastic component (31% at Tarrawarra and 40% at Cache la Poudre for the indirect model compared to 30% and 41%, respectively, for the observations). The indirect model also closely approximates the observed semivariogram shapes. At Tarrawarra, for example, the nugget for π_s^* is 19% of its sill, and the correlation length is approximately 35 m, compared 14% and 31 m, respectively, for $\pi_{s,obs}$. At Tarrawarra, the nugget for π_u^* is 62% of its sill, and the correlation length is approximately 41 m, compared to 62% and 45 m, respectively, for $\pi_{u,obs}$. Overall, these results indicate that the indirect model reproduces the semivariogram features of both the stable and unstable patterns.

The direct model, however, is not able to reproduce the features of stable and unstable semivariograms because it does not introduce any stable patterns. The semivariogram for $\pi_{s,d}^*$ includes slight variance because the temporal-average of the unstable stochastic patterns is not exactly zero. Thus, the decomposition of the generated soil moisture patterns produces a stable pattern with low uncorrelated variance.

Figure 4 plots the semivariogram properties of the modeled stochastic component (π^* and π_d^*) on each date against the associated $\overline{\theta}$. At Tarrawarra, both models produce a relatively constant nugget, which is also seen for the observations. For both models, the constant nugget is caused by e^* and c^* and their additive relationship with $\overline{\theta}$. In the indirect model, for example, e^* enters the final soil moisture equation additively (Equation 31), and each analytical

soil moisture value in the same equation depends on $\bar{\theta}$ (Equations 7-10). The additive relationship implies that the contribution of measurement error remains constant as $\bar{\theta}$ changes. At Cache la Poudre, both models reproduce the positive trend between the nugget and $\bar{\theta}$. In the indirect model, this trend primarily results from p_u^* and its multiplicative relationship with $\bar{\theta}$ (Equations 25 and 27-30). As $\bar{\theta}$ increases, uncorrelated variations in porosity produce a larger nugget in π^*. In the direct model, this positive trend is caused by b^* and its multiplicative relationship with $\bar{\theta}$ (Equation 35). For both catchments, the modeled correlation length does not change with $\bar{\theta}$, which is consistent with the observations. The constant correlation length is determined by the prescribed correlation lengths of the stochastic variations. For both catchments, the models produce a positive trend between partial sill and $\bar{\theta}$. This behavior matches the observations at Tarrawarra but not at Cache la Poudre. In the indirect model, the trend results from p_c^* and d^* and their multiplicative relationships with $\bar{\theta}$. As $\bar{\theta}$ increases, correlated variations in porosity and disequilibrium produce a larger partial sill in π^*. In the direct model, this trend is caused by σ_a and its multiplicative relationship with $\bar{\theta}$.

Figure 5 plots the semivariogram properties of the modeled unstable patterns (π_u^* and $\pi_{u,d}^*$) on each date against the associated $\bar{\theta}$. At both catchments, the indirect model produces a relatively constant nugget as $\bar{\theta}$ changes, which matches the observations. For both models, this behavior is due to the influence of e^* and c^* and their additive relationship with $\bar{\theta}$. However, the direct model produces a slight positive relationship between the nugget and $\bar{\theta}$, which is due to the influence of b^* and its multiplicative relationship with $\bar{\theta}$. At both catchments, the models reproduce the relatively constant correlation lengths. At both catchments, the models are

also able to reproduce the positive trend between partial sill and $\overline{\theta}$. For the indirect model, this trend is primarily due to the influence of d^* and its multiplicative relationship with $\overline{\theta}$. As $\overline{\theta}$ increases, correlated variations in disequilibrium produce a larger partial sill in π_u^*. In the direct model, this trend is caused by a^* and its multiplicative relationship with $\overline{\theta}$.

Example soil-moisture patterns (θ_{obs}, θ, θ^*, and θ_d^*) are shown in Figure 6. The pre-existing EMT+VS model (θ) reproduces the observed dependence on topography (Figure 1) and vegetation. The generalized models maintain much of that dependence but also produce patterns that are more visually similar to the observations. However, the models are not able to reproduce all observed tendencies. At Tarrawarra, for example, the observations have contiguous wet locations in the valleys, while the generalized models have less continuity of these features. Additionally, the observations have a dry patch on the north-facing hillslope that is not fully reproduced by the generalized models. The models' inability to reproduce these features may be caused in part by the use of homogeneous random fields. As expected, the generalized models do not produce wet and dry locations at exactly the right locations, but the tendencies of the modeled patterns are very similar the observations.

Histograms of θ_{obs}, θ, θ^*, and θ_d^* for dry, intermediate, and wet dates are shown in Figure 7. The pre-existing EMT+VS model does not reproduce the observed histograms of soil moisture or the extreme values of soil moisture in the catchments. Both the indirect and direct models are able to reproduce the histogram shape on all three dates at both catchments.

Example lower and upper confidence limits from the indirect and direct models are shown in Figure 8 for an example date. The lower limit represents the 10th percentile and the upper limit represents the 90th percentile of soil moisture. The indirect and direct models

produce almost the same confidence interval maps. However, the difference between the upper and lower limit (i.e. confidence interval) is not equal for all fine-resolution locations on a given date. Although each new stochastic variable is homogeneous, the spatial heterogeneity of the confidence interval indicates that the modeled stochastic patterns (π^* and π_d^*) are heterogeneous. In the indirect model, this heterogeneity is caused by spatial variations in vegetation and topography. In the direct model, this heterogeneity is directly proportional to the pre-existing EMT+VS model estimate θ. Both models produce narrower confidence intervals at dry locations and wider intervals at wet locations.

Figure 9 plots the percentage of the soil moisture observations from all dates that fall within the confidence intervals (y-axis) as a function of the selected confidence level (x-axis). At Tarrawarra, too many observations fall within the confidence intervals for both models when the selected interval is less than 90%. If the selected confidence interval is 50%, for example, about 56% of the observations fall within the specified range. These confidence intervals are too wide because the modeled soil moisture distribution does not perfectly match the observed distribution. The accuracy of the confidence interval improves for larger confidence levels. At Cache la Poudre, the confidence interval error is less than 2% for all confidence levels considered.

Figure 10 shows the temporal-average statistical moments (standard deviation, skewness, and kurtosis) of θ_{obs}, θ, θ^*, and θ_d^*. The pre-existing EMT+VS model substantially underestimates standard deviation, while the generalized models very closely reproduce the observed standard deviation. At Tarrawarra, the pre-existing EMT+VS model does not accurately reproduce skewness and kurtosis, while the indirect and direct models more closely reproduce these statistics (with the indirect model performing slightly better). At Cache la

Poudre, both models can approximate the observed statistics (again with the indirect model performing slightly better), but the improvement upon the pre-existing EMT+VS model is more difficult to see.

4.4 Uncalibrated Model Results

The previous section showed that the generalized models can reproduce nearly all the observed statistical properties if the models are calibrated with local soil moisture observations. In many practical circumstances, however, sufficient data may not be available to allow catchment-specific calibration. This section examines the performance of the indirect and direct models if they are applied to the Nerrigundah and Satellite Station catchments without any local calibration for the indirect and direct model parameters. The parameters for the generalized EMT+VS models are estimated by taking the average between the calibrated parameters at Tarrawarra and Cache la Poudre (see average columns in Table 2 and Table 3). The calibrated parameters for the pre-existing EMT+VS model (Table 1) were used to estimate θ.

The temporal-average semivariograms for the modeled soil moisture (θ^* and θ_d^*) and the associated stochastic component (π^* and π_d^*) at Nerrigundah and Satellite Station are shown in Figure 11. At Nerrigundah, both models produce almost identical results and underestimate the variance in the soil moisture and its stochastic component for all lag distances. At Satellite Station, both models produce semivariograms that roughly approximate the observed semivariograms, but the indirect model performs slightly better.

The semivariograms for the modeled stable patterns (π_s^* and $\pi_{s,d}^*$) and the temporal-average semivariograms for the unstable patterns (π_u^* and $\pi_{u,d}^*$) at Nerrigundah and Satellite Station are shown in Figure 12. For both catchments, the observed stable patterns represent a

larger portion of the stochastic variance than the unstable patterns (in contrast to Tarrawarra and Cache la Poudre). At Nerrigundah, the indirect model reproduces the unstable patterns, but it underestimates the contribution of the stable pattern. At Satellite Station, the indirect model roughly reproduces the semivariograms for both the stable and unstable patterns. The direct model does not reproduce the semivariograms for the stable and unstable patterns because it does not include any stable stochastic variables.

The plots comparing semivariogram properties to $\overline{\theta}$ are not shown for the model validation. Because of the narrow range of most average soil-moisture values at Nerrigundah and the small number of sample dates at Satellite Station, no clear trends are visible in the observations. Thus, the ability of the generalized EMT+VS models to match the observations is difficult to interpret.

Example soil-moisture patterns (θ_{obs}, θ, θ^*, and θ_d^*) for Nerrigundah and Satellite Station are shown in Figure 13. Similar to Tarrawarra and Cache la Poudre, the pre-existing EMT+VS model is able to reproduce the dependence on topography (Figure 1). The generalized models maintain much of that dependence but also produce patterns that are more visually similar to the observations. At Satellite Station, the observed pattern exhibits more spatially continuous wet locations in the valleys than the patterns produced by the generalized models.

Histograms of θ_{obs}, θ, θ^*, and θ_d^* for dry, intermediate, and wet dates at Nerrigundah and Satellite Station are shown in Figure 14. The pre-existing EMT+VS model again does not reproduce the observed histograms of soil moisture, and it does not capture the extreme values of soil moisture in the catchments. Both the indirect and direct models are able to approximate the histogram shapes for all three dates despite the flaws in their semivariograms that were observed earlier.

The performance of the indirect and direct model confidence intervals is shown in Figure 15. At Nerrigundah, both models consistently underestimate the confidence interval because they underestimate the variance of stochastic component at this site. At Satellite station, the confidence intervals are relatively accurate (and the indirect model performs better than the direct model) for confidence levels smaller than about 80%. Above this level, the confidence interval is underestimated (and the direct model performs better).

Figure 16 shows the temporal-average statistical moments (standard deviation, skewness, and kurtosis) of θ_{obs}, θ, θ^*, and θ_d^*. The pre-existing EMT+VS model substantially underestimates standard deviation, while the generalized models more closely reproduce the observed standard deviation. At Nerrigundah, both generalized models underestimate the observed standard deviation, which is because the parameters controlling the standard deviation of stochastic variations are uncalibrated. At Satellite Station, the indirect and direct models very accurately reproduce the observed standard deviation. Although uncalibrated parameters are used at Nerrigundah and Satellite Station, the generalized models are able to approximate all of the observed statistical moments more accurately than the pre-existing EMT+VS model.

5. CONCLUSIONS

The primary objectives of this study were (1) to characterize the stochastic variability of soil moisture at the catchment scale and (2) to develop downscaling models that reproduce the observed statistical features of soil moisture. The stochastic variations in soil moisture were obtained by removing the dependence on site properties such as topography and vegetation from soil-moisture observations. These variations were then decomposed into a stable pattern (that can be present to some extent on every date) and unstable patterns that vary through time. Geostatistical analysis was then used to analyze each of those patterns. Two downscaling models were developed to include stochastic variations in soil moisture. In the indirect model, stochastic variations were introduced through porosity perturbations, deviations from equilibrium moisture, and measurement errors. In the direct model, the stochastic variations were directly introduced into the final soil moisture values. The following conclusions can be made from the results:

1. The stochastic component of soil moisture represents a substantial portion of the overall soil-moisture variation. The sill of the stochastic component is on average approximately 64% and 84% of the sill of overall soil moisture at Tarrawarra and Cache la Poudre, respectively. Thus, a majority of the variation at both catchments can be considered stochastic.
2. The stochastic component exhibits non-trivial semivariogram features (i.e. a nonzero nugget, correlation length, and partial sill). The presence of a nonzero nugget and partial sill indicates that the stochastic component includes both correlated and uncorrelated patterns. At both catchments, the nugget is on average about half of the total sill, which

implies that the correlated and uncorrelated patterns contribute about equal variation on average.

3. The semivariogram of the stochastic component also depends on the spatial-average soil moisture. At Tarrawarra, the nugget remains relatively constant while the partial sill increases with spatial-average soil moisture. At Cache la Poudre, the nugget increases with spatial-average soil moisture, while the partial sill remains relatively constant. The correlation length remains approximately constant at both catchments.
4. The stochastic variations also include a temporally stable pattern with substantial variability. The sill of the stable pattern is 30% and 41% of the sill of the stochastic component at Tarrawarra and Cache la Poudre, respectively. The stable patterns at both catchments also exhibit nonzero nuggets and partial sills, which indicate contributions from both correlated and uncorrelated patterns.
5. The semivariograms of the unstable patterns depend on the spatial-average soil moisture, and this dependence is similar at both catchments. In particular, the nugget and the correlation length remain relatively constant, while the partial sill increases with spatial-average soil moisture.
6. The indirect downscaling model is able to reproduce nearly all the observed statistical features for the catchments where its stochastic parameters were calibrated. Specifically, it reproduces the semivariograms of the soil moisture, stochastic component, stable pattern, and unstable patterns. It also reproduces the appropriate dependencies on the spatial-average soil moisture (aside from the partial sill of the stochastic component at Cache la Poudre). In addition, the indirect model adequately reproduces the soil moisture histograms for both catchments. At low confidence levels, the indirect model's

confidence intervals can include as much as 6% too many observations. However, the intervals become more accurate for larger confidence levels.

7. The direct model produces very similar results to the indirect model except that it does not distinguish between stable and unstable patterns. Thus, it is unable to reproduce the semivariograms for the stable pattern and the unstable patterns.
8. Both models provide only approximate results when they are not calibrated to local observations. In particular, the semivariograms produced by the models include substantial errors at Nerrigundah but perform better at Satellite Station. For both catchments, however, the soil moisture histograms and confidence limits remain relatively accurate. Thus, the models cannot simulate realistic spatial patterns without calibration, but they may still be able to approximate the overall soil moisture frequency distribution.

Two main avenues are open for future research. First, similar analyses should be performed using additional catchments. The physical factors that control the stochastic model parameters (i.e. the standard deviations and correlation lengths) remain unknown. Thus, these parameters currently cannot be estimated without calibration. If additional catchments were analyzed and compared to the present study, the controlling factors might become more clear. Second, similar analyses should be performed on larger regions. Second, similar analyses should be performed using fine-resolution soil moisture data from larger regions. This study considered only soil moisture patterns within small spatial extents (catchments). Soil moisture may exhibit stochastic variations with correlation lengths beyond what can be observed within the spatial extents of catchments.

TABLES AND FIGURES

Table 1. Inputs and parameters for the pre-existing EMT+VS model based on Hoehn (2016) and Hoehn et al. (2017). All inputs and parameters were calibrated except those marked by an asterisk, which were directly specified. Parameters without provided units are dimensionless.

Category	Parameter	Symbol (units)	Tarrawarra	Cache la Poudre	Nerrigundah	Satellite Station
Climate	Coarse potential ET	E_p (mm/day)	2.25*	2.55*	2.81*	2.28*
	Priestly-Taylor coefficient minus one	α	0.26*	0.26*	0.26*	0.26*
Climate & Vegetation	Aerodynamic ET exponent	β_a	5	3.60	5	1
	Radiation ET exponent	β_r	3.55	5	1.60	5
Vegetation	Interception efficiency	λ	0.37	0.89	0.96	0.40
	Portion of transpiration from soil layer	η	0.83	0.04	1	0.10
	Shading effect on soil evaporation	μ	1*	1.92	1*	1*
Soil Thickness	Layer thickness where topographic curvature is zero	δ_0 (m)	0.3*	0.05*	0.25*	1*
	Minimum curvature where layer is present	$\kappa_{\min}$ (1/m)	-886375	-651810	-643233	-660661
Soil Hydraulics	Porosity	ϕ (m^3/m^3)	0.70	0.409	0.435	0.484
	Vertical saturated hydraulic conductivity	$K_{s,v}$ (mm/day)	386.3	984.9	36.0	59.0
	Horizontal pore disconnectedness index	γ_h	6.92	14.36	5.01	8.31
	Vertical pore disconnectedness index	γ_v	14.12	14.10	29.15	15.74
	Anisotropy of saturated hydraulic conductivity	ι	47.2	75.4	209	500
	Relation of hydraulic to topographic gradient	ε	1.00	3.00	1.00	2.38

Table 2. Manually calibrated parameters for the indirect model. Parameters without units are dimensionless.

Category	Parameter	Symbol (units)	Tarrawarra	Cache la Poudre	Average
Porosity	Correlated porosity standard deviation	σ_{p_c}	0.040	0.11	0.075
	Porosity correlation length	ρ_p (m)	42 m	38 m	40 m
	Uncorrelated porosity standard deviation	σ_{p_u}	0.006	0.122	0.064
Disequilibrium	Correlated disequilibrium standard deviation	σ_d	0.041	0.108	0.075
	Disequilibrium correlation length	ρ_d (m)	52 m	20 m	36 m
Measurement Error	Measurement error standard deviation	σ_e	0.019	0.018	0.019

Table 3. Manually calibrated parameters for the direct model. Parameters without units are dimensionless.

Category	Parameter	Symbol (units)	Tarrawarra	Cache la Poudre	Average
Multiplicative	Correlated standard deviation	σ_a	0.057	0.140	0.099
	Correlation length	ρ_a (m)	42 m	31 m	37 m
	Uncorrelated standard deviation	σ_b	0.028	0.120	0.074
Additive	Measurement error standard deviation	σ_c	0.016	0.020	0.018

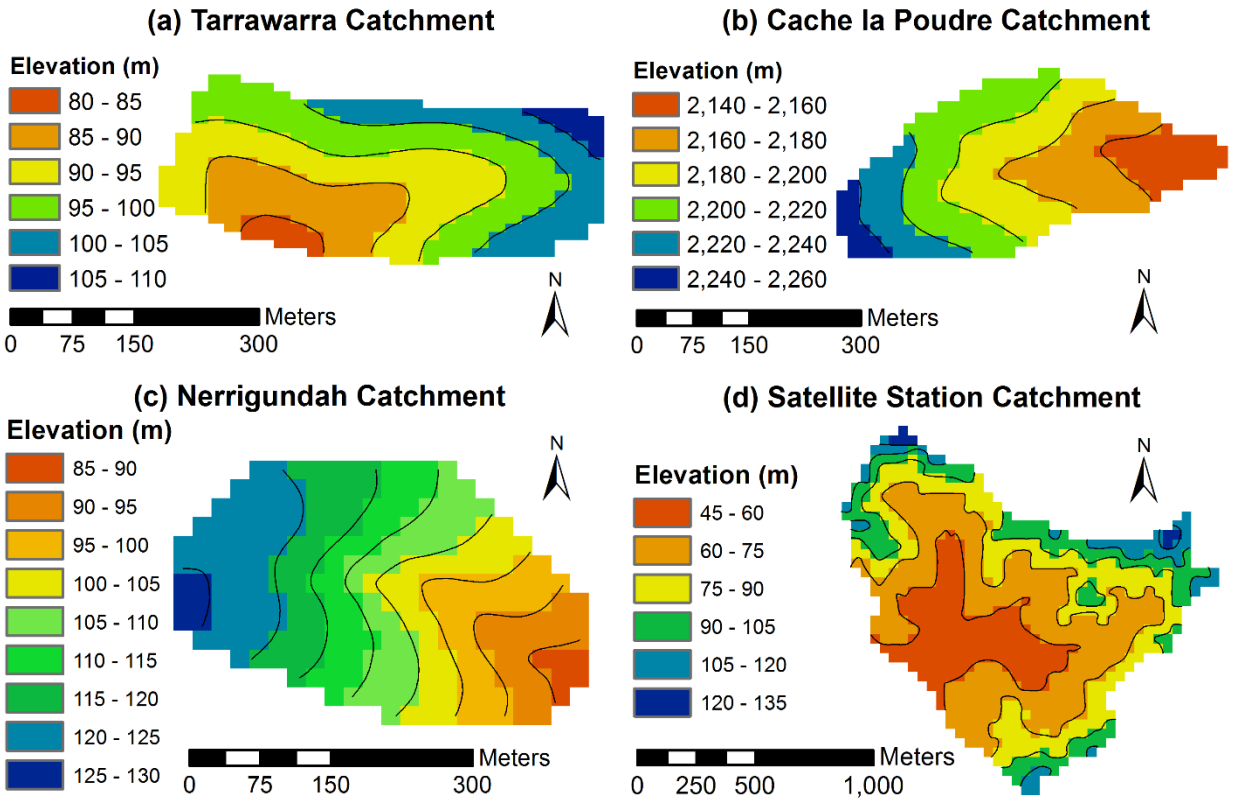

Figure 1. Elevation maps of the two analysis catchments (a) Tarrawarra and (b) Cache la Poudre and the two evaluation catchments (c) Nerrigundah and (d) Satellite Station.

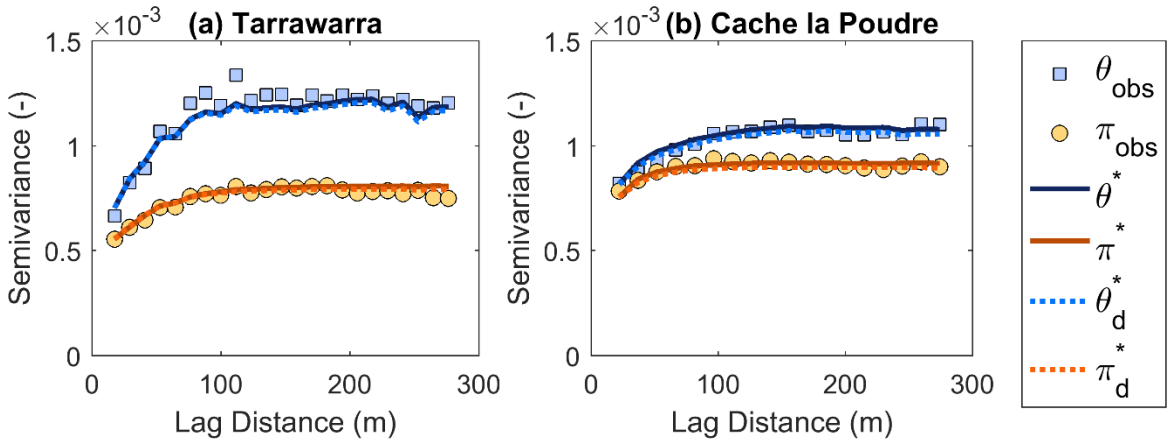

Figure 2. Semivariograms of observed soil moisture θ_{obs}, observed stochastic component π_{obs}, indirect model soil moisture θ^*, indirect model stochastic component π^*, direct model soil moisture θ_d^*, and direct model stochastic component π_d^* at (a) Tarrawarra and (b) Cache la Poudre. These semivariograms are the average of all sample dates' semivariograms.

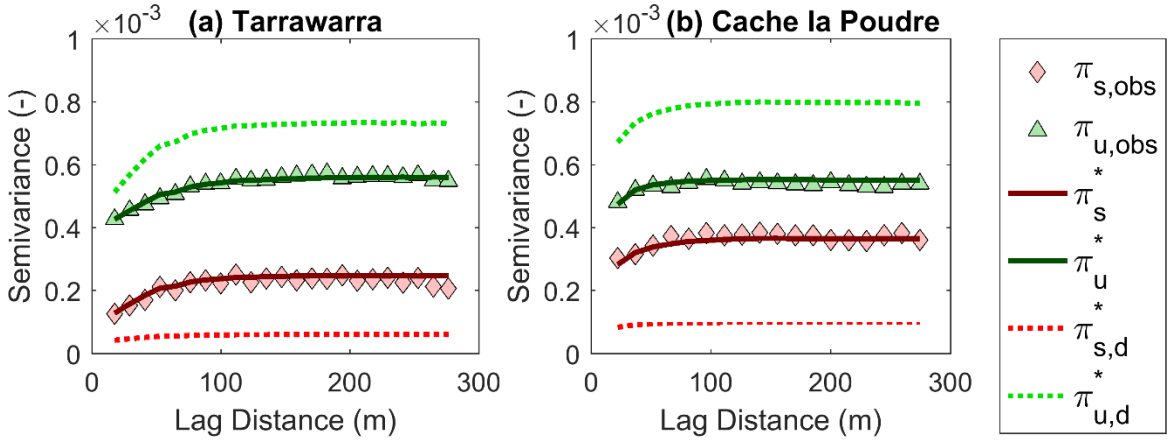

Figure 3. Semivariograms of observed stable stochastic pattern $\pi_{s,obs}$, observed unstable stochastic patterns $\pi_{u,obs}$, indirect model stable pattern π_s^*, indirect model unstable patterns π_u^*, direct model stable pattern $\pi_{s,d}^*$, and direct model unstable patterns $\pi_{u,d}^*$ at (a) Tarrawarra and (b) Cache la Poudre. The semivariograms for the unstable patterns are the average of all sample dates' semivariograms.

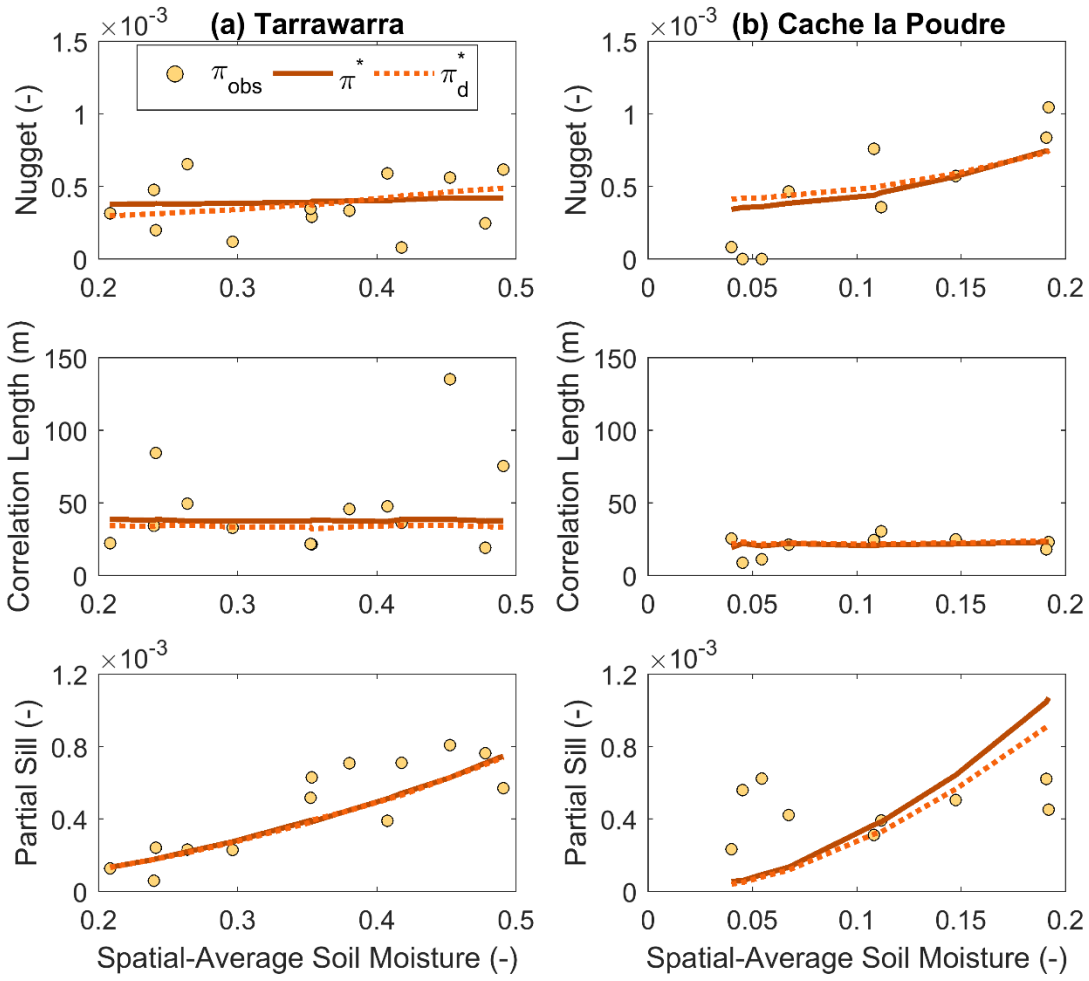

Figure 4. Scatter plots of the nugget, correlation length, and partial sill of the observed stochastic component of soil moisture π_{obs}, indirect model stochastic component π^*, and direct model stochastic component π_d^* as a function of spatial-average soil moisture at (a) Tarrawarra and (b) Cache la Poudre.

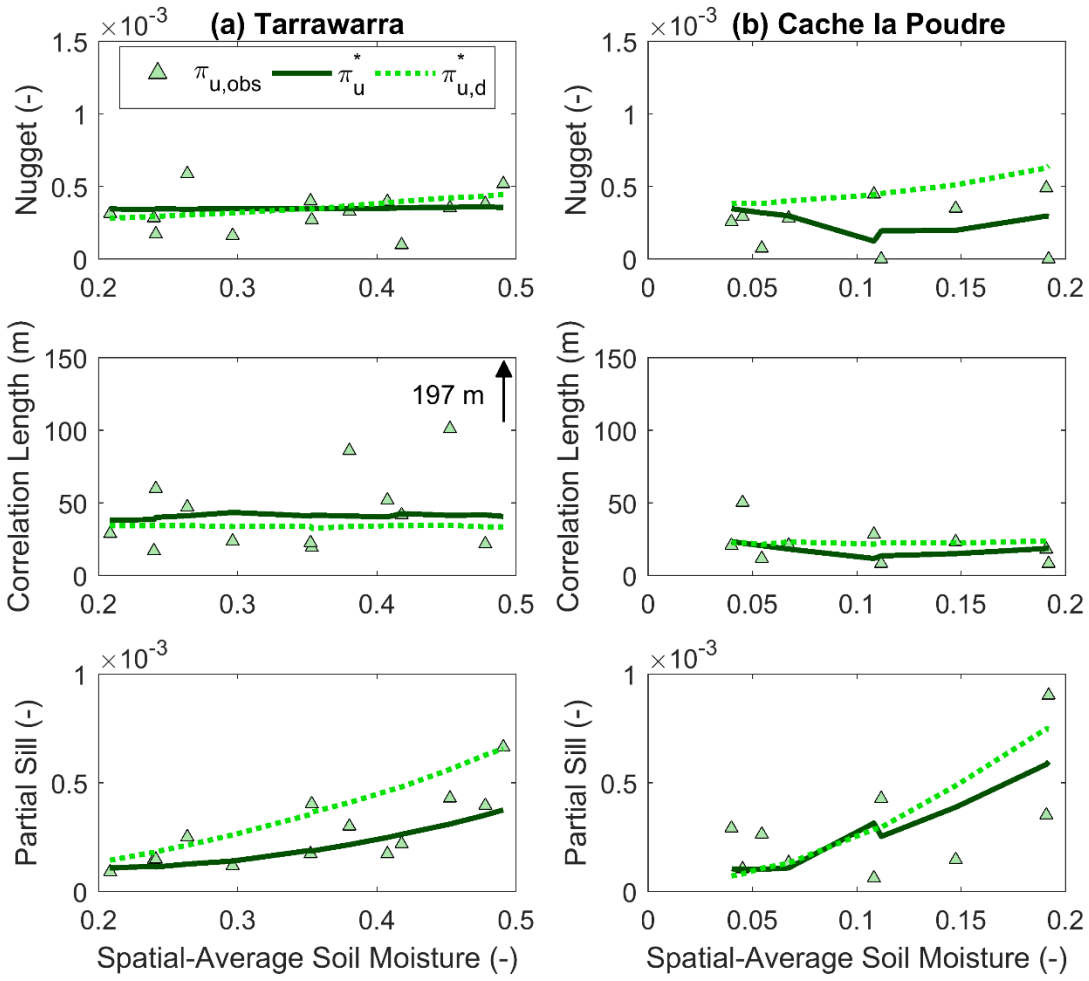

Figure 5. Scatter plots of the nugget, correlation length, and partial sill of the observed unstable patterns $\pi_{u,obs}$, indirect model unstable patterns π_u^*, and direct model unstable patterns $\pi_{u,d}^*$ as a function of the spatial-average soil moisture at (a) Tarrawarra and (b) Cache la Poudre. The arrow represents a sample date with a correlation length of 197 m for $\pi_{u,obs}$.

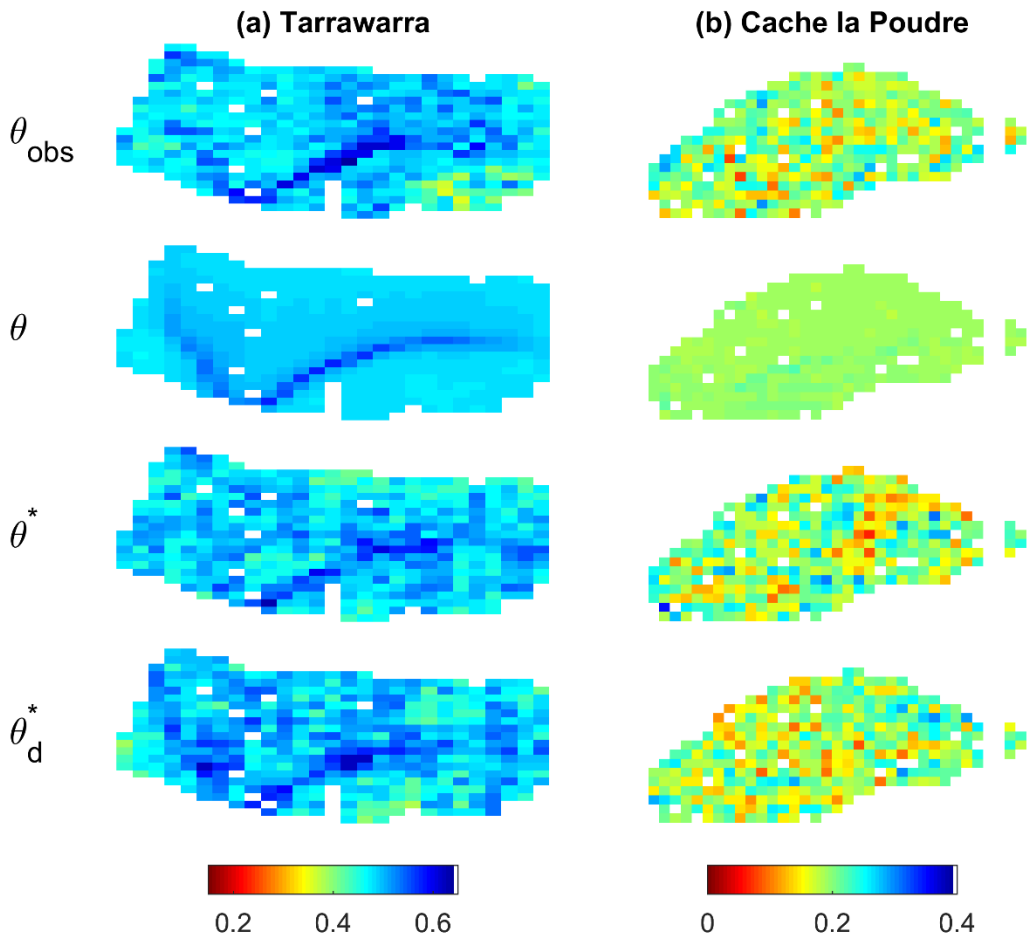

Figure 6. Example maps of observed soil moisture θ_{obs}, pre-existing EMT+VS model estimate θ, indirect model soil moisture θ^*, and direct model soil moisture θ_d^* at (a) Tarrawarra on 02-Sep-96 and (b) Cache la Poudre on 28-May-08.

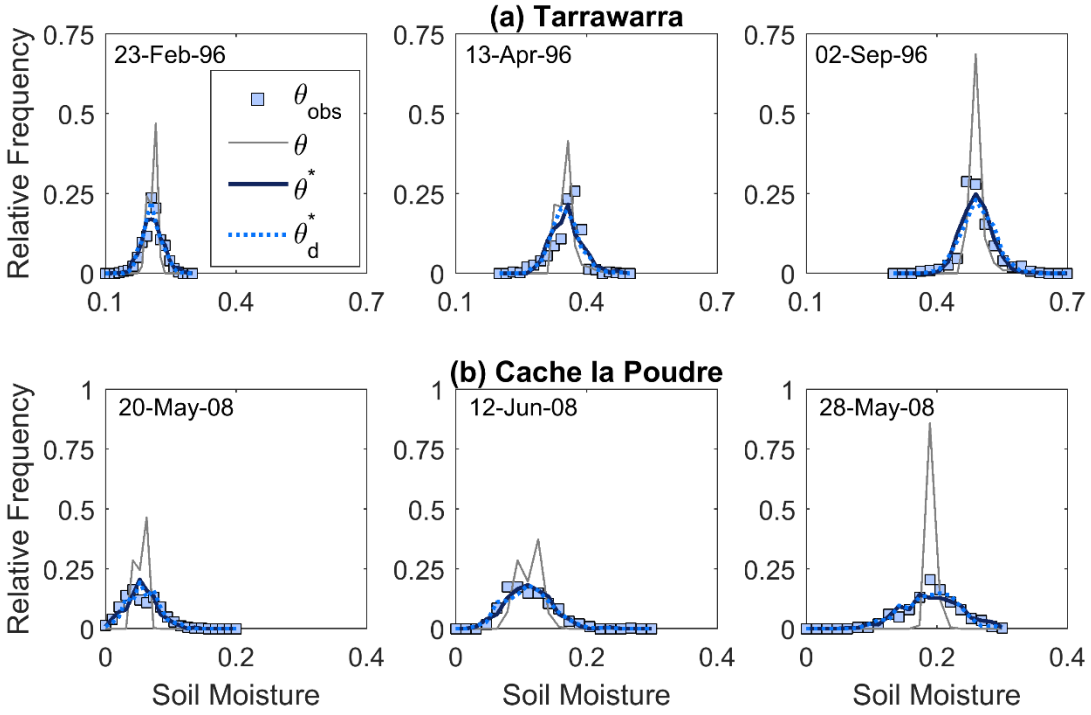

Figure 7. Example histograms of observed soil moisture θ_{obs}, pre-existing EMT+VS model estimate θ, indirect model soil moisture θ^*, and direct model soil moisture θ_d^* on a dry, intermediate, and wet date at (a) Tarrawarra and (b) Cache la Poudre.

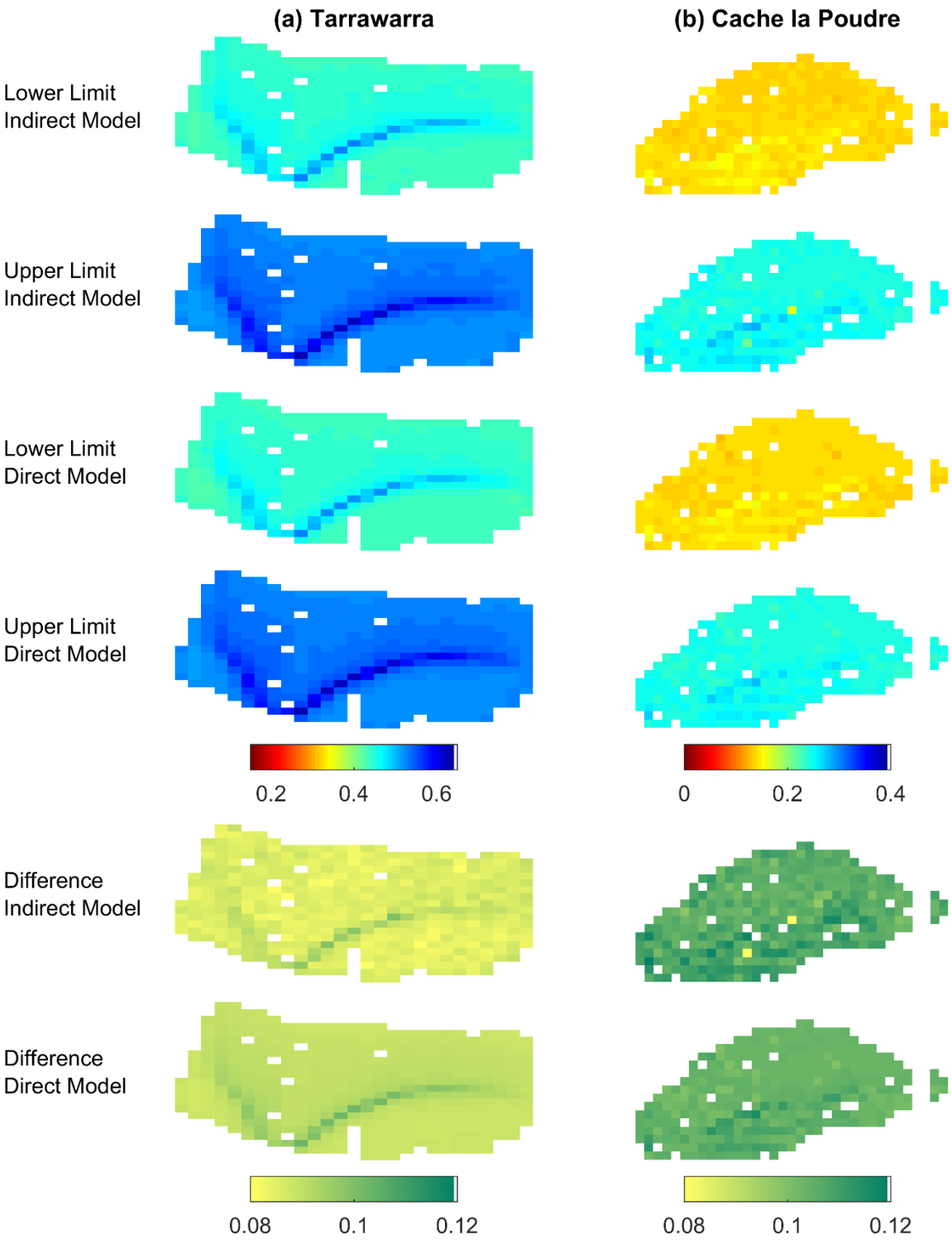

Figure 8. Example 80% confidence limits on soil-moisture and the difference between the upper and lower limits at (a) Tarrawarra on 02-Sep-96 and (b) Cache la Poudre on 28-May-08. Lower limit represents the 10% quantile, the upper limit represents the 90% quantile.

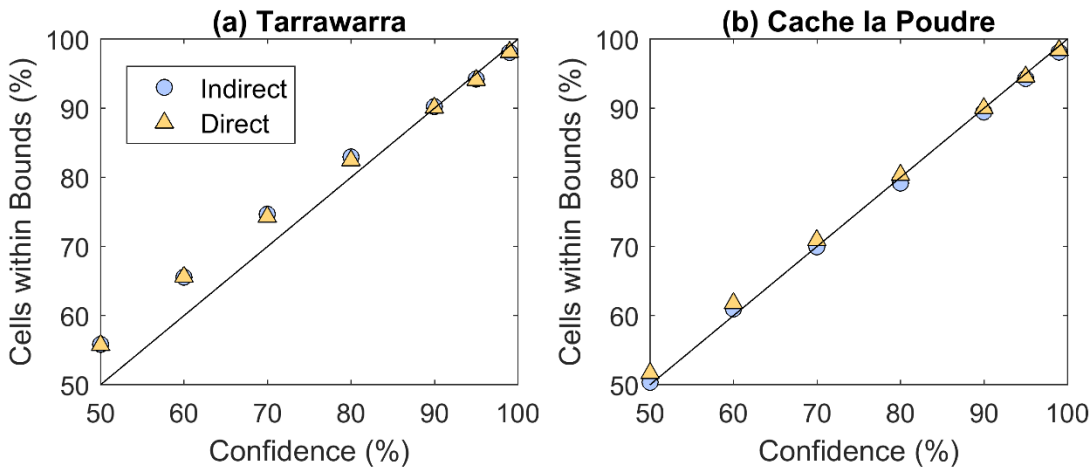

Figure 9. Evaluation of estimated confidence intervals by comparing the percentage of observations within the bounds (y-axis) at the selected confidence levels (x-axis) at (a) Tarrawarra and (b) Cache la Poudre averaged for all sample dates.

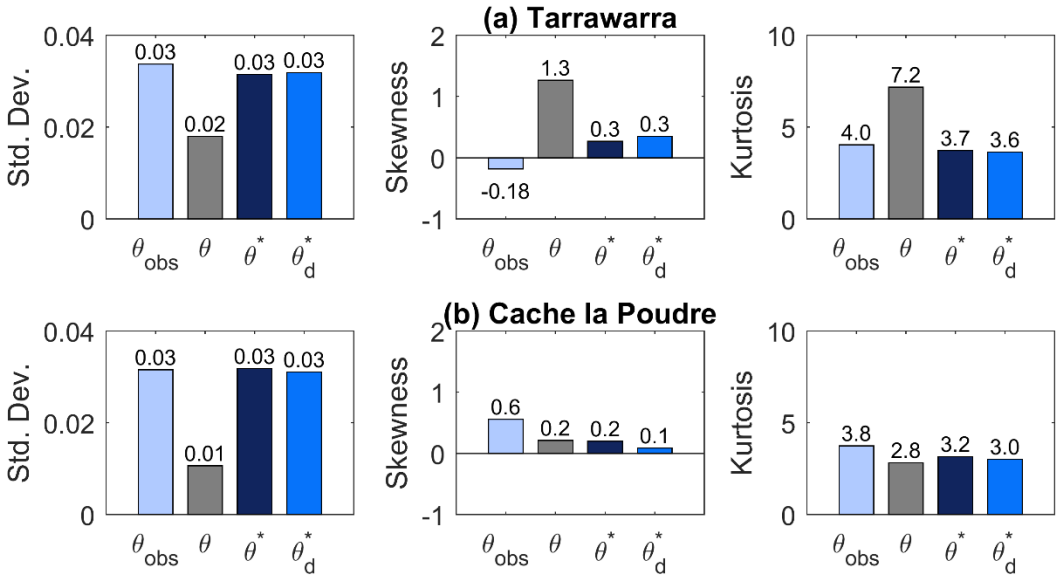

Figure 10. Average statistical moments (standard deviation, skewness, and kurtosis) of observed soil moisture θ_{obs}, pre-existing EMT+VS model estimate θ, indirect model soil moisture θ^*, and direct model soil moisture θ_d^* at (a) Tarrawarra and (b) Cache la Poudre.

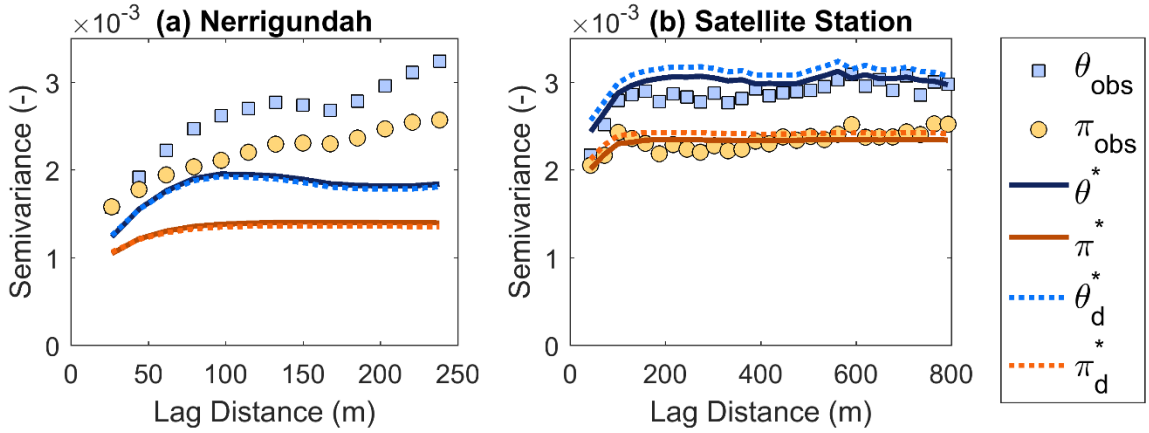

Figure 11. Semivariograms of the observed soil moisture θ_{obs}, observed stochastic component π_{obs}, indirect model soil moisture θ^*, indirect model stochastic component π^*, direct model soil moisture θ_d^*, and direct model stochastic component π_d^* at (a) Nerrigundah and (b) Satellite Station. These semivariograms are the average of all sample dates' semivariograms.

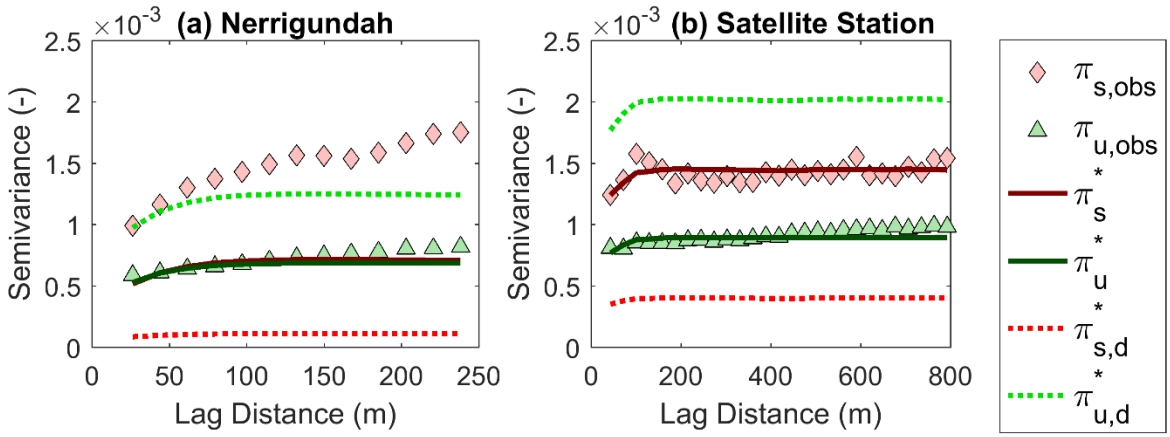

Figure 12. Semivariograms of observed stable pattern $\pi_{s,obs}$, observed unstable pattern $\pi_{u,obs}$, indirect model stable pattern π_s^*, indirect model unstable pattern π_u^*, direct model stable pattern $\pi_{s,d}$, and direct model unstable pattern $\pi_{u,d}$ at (a) Nerrigundah and (b) Satellite Station. The semivariograms for the unstable patterns are the average of all sample dates' semivariograms.

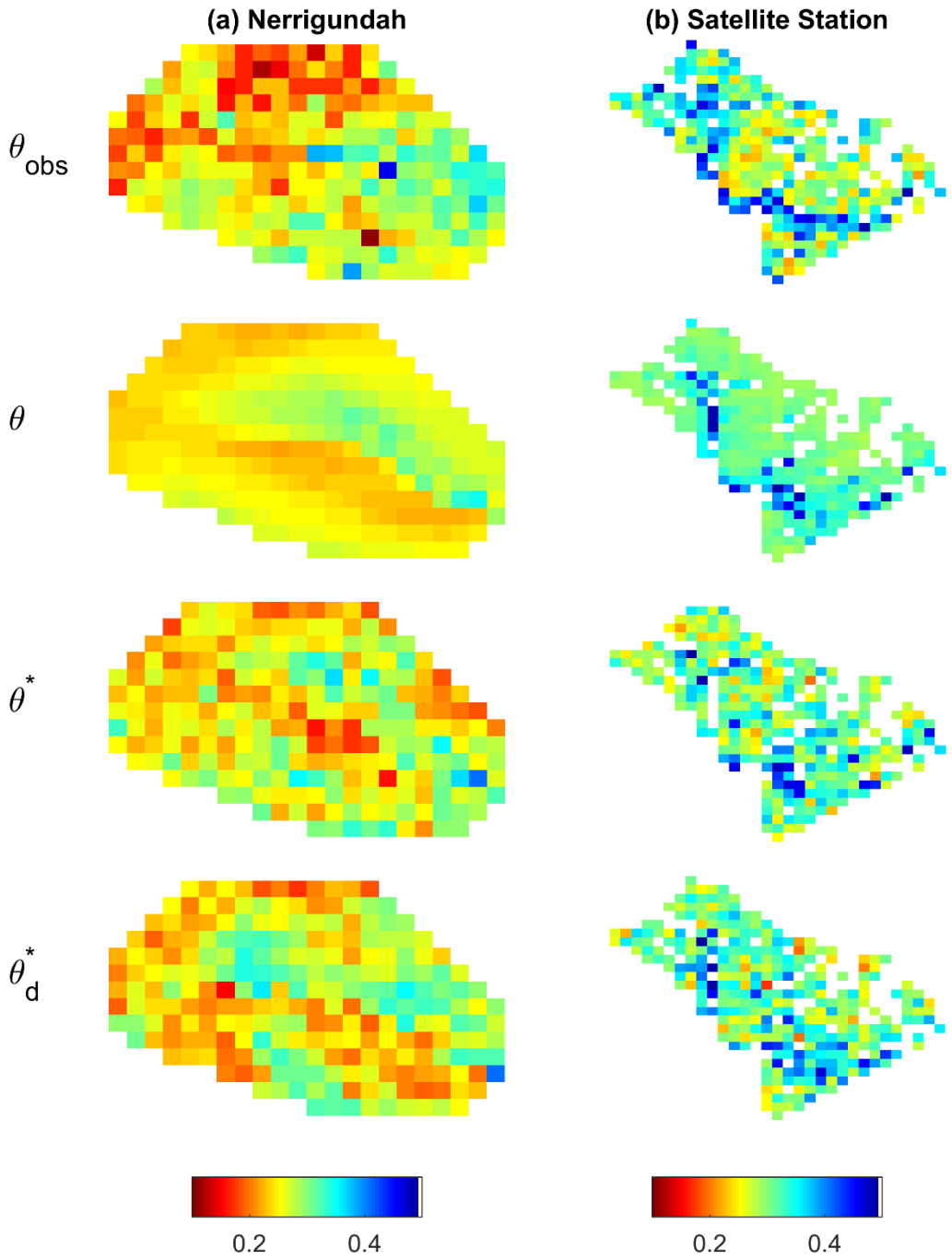

Figure 13. Example maps of observed soil moisture θ_{obs}, pre-existing EMT+VS model estimate θ, indirect model soil moisture θ^*, and direct model soil moisture θ_d^* at (a) Nerrigundah on 27-Aug-97 and (b) Satellite Station on 25-Mar-98.

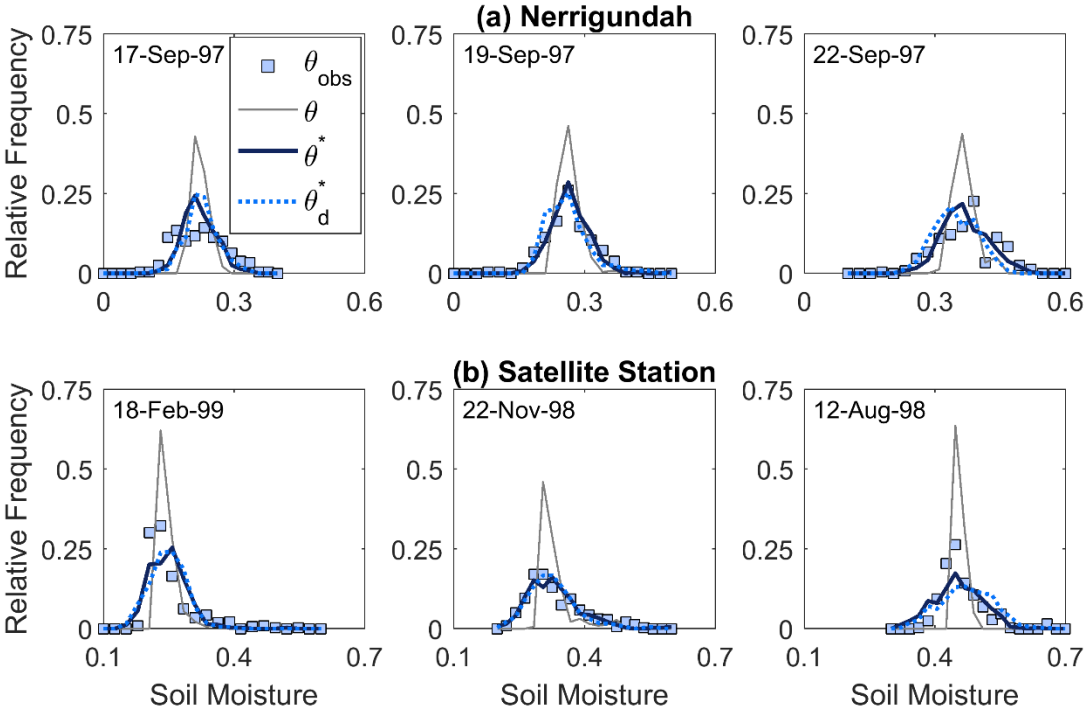

Figure 14. Example histograms of observed soil moisture θ_{obs}, pre-existing EMT+VS model estimate θ, indirect model soil moisture θ^*, and direct model soil moisture θ_d^* on a dry, intermediate, and wet date at (a) Nerrigundah and (b) Satellite Station.

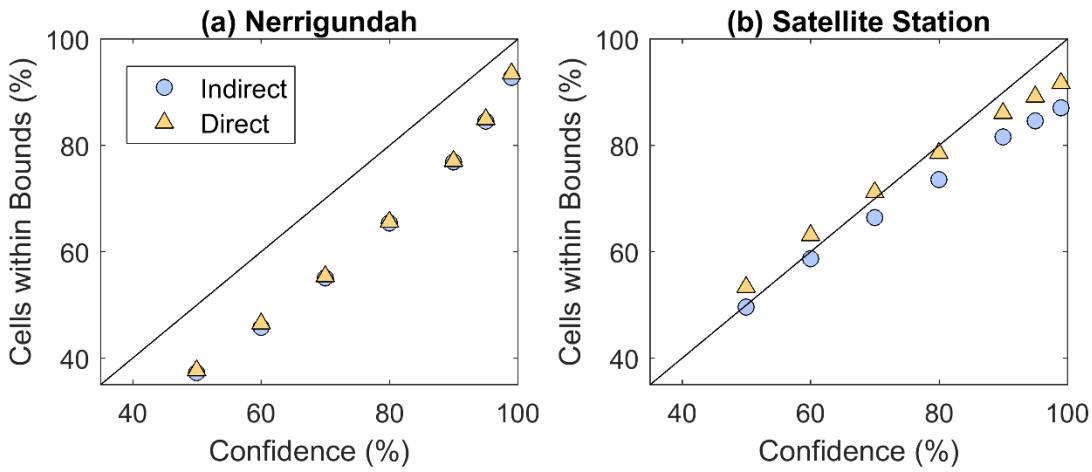

Figure 15. Evaluation of estimated confidence intervals by comparing the percentage of observations within the bounds (x-axis) at the selected confidence levels (y-axis) at (a) Nerrigundah and (b) Satellite Station averaged for all sample dates.

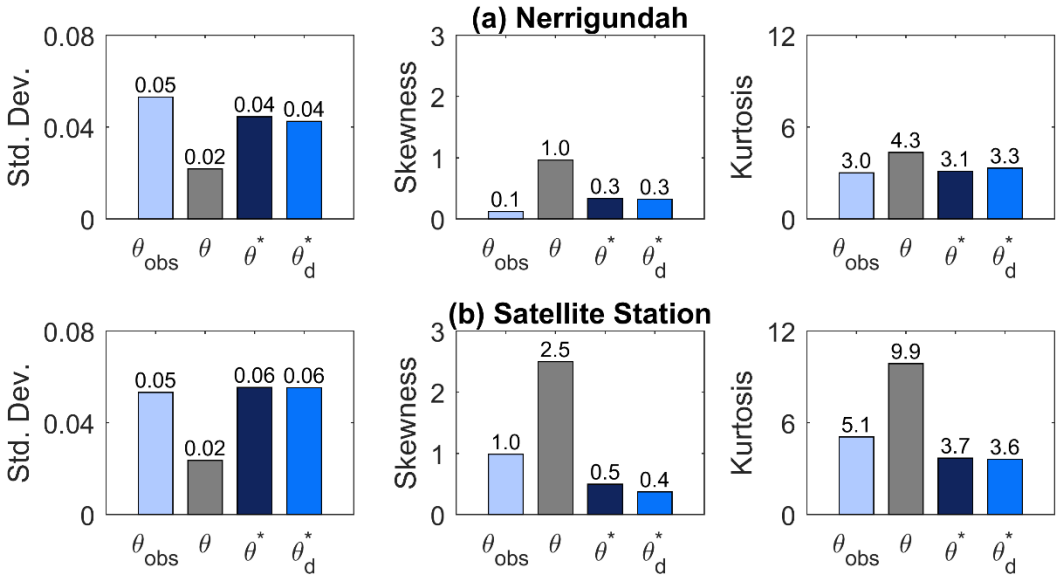

Figure 16. Average statistical moments (standard deviation, skewness, and kurtosis) of observed soil moisture θ_{obs}, pre-existing EMT+VS model estimate θ, indirect model soil moisture θ^*, and direct model soil moisture θ_d^* at (a) Nerrigundah and (b) Satellite Station.

REFERENCES

Bakr, A.A., Gelhar, L.W., Gutjahr, A.L., Macmillan, J.R., 1978. Stochastic Analysis of Spatial Variability in Subsurface Flows .1. Comparison of One-Dimensional and 3-Dimensional Flows. Water Resour Res, 14(2): 263-271. doi: 10.1029/Wr014i002p00263

Bakr, A.A.M., 1976. Stochastic analysis of the effect of spatial variations of hydraulic conductivity on groundwater flow, New Mexico Institute of Mining and Technology.

Bartsch, A., Balzter, H., George, C., 2009. The influence of regional surface soil moisture anomalies on forest fires in Siberia observed from satellites. Environ Res Lett, 4(4). doi: 10.1088/1748-9326/4/4/045021

Beven, K.J., Kirkby, M.J., 1979. A physically based, variable contributing area model of basin hydrology / Un modèle à base physique de zone d'appel variable de l'hydrologie du bassin versant. Hydrological Sciences Bulletin, 24(1): 43-69. doi: 10.1080/02626667909491834

Brocca, L., Morbidelli, R., Melone, F., Moramarco, T., 2007. Soil moisture spatial variability in experimental areas of central Italy. J Hydrol, 333(2-4): 356-373. doi: 10.1016/j.jhydrol.2006.09.004

Busch, F.A., Niemann, J.D., Coleman, M., 2012. Evaluation of an empirical orthogonal function-based method to downscale soil moisture patterns based on topographical attributes. Hydrol Process, 26(18): 2696-2709. doi: 10.1002/hyp.8363

Campbell, G.S., 1974. Simple Method for Determining Unsaturated Conductivity from Moisture Retention Data. Soil Sci, 117(6): 311-314.

Chen, C.F., Son, N.T., Chang, L.Y., Chen, C.C., 2011. Monitoring of soil moisture variability in relation to rice cropping systems in the Vietnamese Mekong Delta using MODIS data. Appl Geogr, 31(2): 463-475. doi: 10.1016/j.apgeog.2010.10.002

Choi, M., Jacobs, J.M., 2007. Soil moisture variability of root zone profiles within SMEX02 remote sensing footprints. Adv Water Resour, 30(4): 883-896. doi: 10.1016/j.advwatres.2006.07.007

Coleman, M.L., Niemann, J.D., 2013. Controls on topographic dependence and temporal instability in catchment-scale soil moisture patterns. Water Resour Res, 49(3): 1625-1642. doi: 10.1002/wrcr.20159

Cowley, G.S., Niemann, J.D., Green, T.R., Seyfried, M.S., Jones, A.S., Grazaitis, P.J., 2017. Impacts of precipitation and potential evapotranspiration patterns on downscaling soil moisture in regions with large topographic relief. Water Resour Res, 53(2): 1553-1574. doi: 10.1002/2016WR019907

Cressie, N., 1985. Fitting Variogram Models by Weighted Least-Squares. J Int Ass Math Geol, 17(5): 563-586. doi: 10.1007/Bf01032109

Crow, W., Dong, J., Tobin, K., Torres, R., 2017. SMERGE: A multi-decadal root-zone soil moisture product for CONUS, AGU Fall Meeting Abstracts.

Cunnane, C., 1978. Unbiased plotting positions—a review. J Hydrol, 37(3-4): 205-222.

De Lannoy, G.J.M., Verhoest, N.E.C., Houser, P.R., Gish, T.J., Van Meirvenne, M., 2006. Spatial and temporal characteristics of soil moisture in an intensively monitored agricultural field (OPE3). J Hydrol, 331(3-4): 719-730. doi: 10.1016/j.jhydrol.2006.06.016

de Wit, A.M., van Diepen, C.A., 2007. Crop model data assimilation with the Ensemble Kalman filter for improving regional crop yield forecasts. Agr Forest Meteorol, 146(1-2): 38-56. doi: 10.1016/j.agrformet.2007.05.004

Dingman, S.L., 2002. Physical Hydrology. Prentice Hall.

Dolloff, J., Doucette, P., 2014. The Sequential Generation of Gaussian Random Fields for Applications in the Geospatial Sciences. Isprs Int Geo-Inf, 3(2): 817-852.

Duffera, M., White, J.G., Weisz, R., 2007. Spatial variability of Southeastern US Coastal Plain soil physical properties: Implications for site-specific management. Geoderma, 137(3-4): 327-339. doi: 10.1016/j.geoderma.2006.08.018

Entekhabi, D. et al., 2010. The Soil Moisture Active Passive (SMAP) Mission. P Ieee, 98(5): 704-716. doi: 10.1109/Jproc.2010.2043918

Famiglietti, J.S., Devereaux, J.A., Laymon, C.A., Tsegaye, T., Houser, P.R., Jackson, T.J., Graham, S.T., Rodell, M., van Oevelen, P.J., 1999. Ground-based investigation of soil moisture variability within remote sensing footprints during the Southern Great Plains 1997 (SGP97) Hydrology Experiment. Water Resour Res, 35(6): 1839-1851. doi: 10.1029/1999wr900047

Famiglietti, J.S., Rudnicki, J.W., Rodell, M., 1998. Variability in surface moisture content along a hillslope transect: Rattlesnake Hill, Texas. J Hydrol, 210(1-4): 259-281. doi: 10.1016/s0022-1694(98)00187-5

Famiglietti, J.S., Ryu, D.R., Berg, A.A., Rodell, M., Jackson, T.J., 2008. Field observations of soil moisture variability across scales. Water Resour Res, 44(1). doi: 10.1029/2006wr005804

Flores, A.N., Entekhabi, D., Bras, R.L., 2014. Application of a hillslope-scale soil moisture data assimilation system to military trafficability assessment. J Terramechanics, 51: 53-66. doi: 10.1016/j.jterra.2013.11.004

Gaur, N., Mohanty, B.P., 2016. Land-surface controls on near-surface soil moisture dynamics: Traversing remote sensing footprints. Water Resour Res, 52(8): 6365-6385.

Grayson, R.B., Western, A.W., Chiew, F.H.S., Bloschl, G., 1997. Preferred states in spatial soil moisture patterns: Local and nonlocal controls. Water Resour Res, 33(12): 2897-2908. doi: 10.1029/97wr02174

Green, T.R., Erskine, R.H., 2004. Measurement, scaling, and topographic analyses of spatial crop yield and soil water content. Hydrol Process, 18(8): 1447-1465. doi: 10.1002/Hyp.1422

Heimsath, A.M., Dietrich, W.E., Nishiizumi, K., Finkel, R.C., 1999. Cosmogenic nuclides, topography, and the spatial variation of soil depth. Geomorphology, 27(1-2): 151-172. doi: 10.1016/S0169-555x(98)00095-6

Hoehn, D.C., 2016. Downscaling soil moisture over regions that include multiple coarse-resolution grid cells, Colorado State University, 54 pp.

Hoehn, D.C., Niemann, J.D., Green, T.R., Jones, A.S., Grazaitis, P.J., 2017. Downscaling soil moisture over regions that include multiple coarse-resolution grid cells. Remote Sens Environ, 199: 187-200. doi: 10.1016/j.rse.2017.07.021

Holzman, M.E., Rivas, R., Piccolo, M.C., 2014. Estimating soil moisture and the relationship with crop yield using surface temperature and vegetation index. Int J Appl Earth Obs, 28: 181-192. doi: 10.1016/j.jag.2013.12.006

Horn, R., Fleige, H., 2003. A method for assessing the impact of load on mechanical stability and on physical properties of soils. Soil Till Res, 73(1-2): 89-99.

Hupet, F., Vanclooster, M., 2004. Sampling strategies to estimate field areal evapotranspiration fluxes with a soil water balance approach. J Hydrol, 292(1-4): 262-280. doi: 10.1016/j.jhydrol.2004.01.006

Isotalo, J., 2001. Basics of statistics. Finland: University of Tampere.

Johnson, R.A., Wichern, D., 2002. Multivariate analysis. Wiley Online Library.

Kerr, Y.H. et al., 2010. The SMOS Mission: New Tool for Monitoring Key Elements of the Global Water Cycle. P Ieee, 98(5): 666-687. doi: 10.1109/Jproc.2010.2043032

Kim, G., Barros, A.P., 2002. Downscaling of remotely sensed soil moisture with a modified fractal interpolation method using contraction mapping and ancillary data. Remote Sens Environ, 83(3): 400-413. doi: 10.1016/S0034-4257(02)00044-5

Korres, W. et al., 2015. Spatio-temporal soil moisture patterns - A meta-analysis using plot to catchment scale data. J Hydrol, 520: 326-341. doi: 10.1016/j.jhydrol.2014.11.042

Kumar, P., 1999. A multiple scale state-space model for characterizing subgrid scale variability of near-surface soil moisture. Ieee T Geosci Remote, 37(1): 182-197. doi: 10.1109/36.739153

Lehman, B.M., Niemann, J.D., 2008. Spatial patterns of a semi-arid montane catchment with aspect-dependent vegetation, First International Conference on Hydropedology, State College, Pennsylvania.

Mascaro, G., Vivoni, E.R., Deidda, R., 2010. Downscaling soil moisture in the southern Great Plains through a calibrated multifractal model for land surface modeling applications. Water Resour Res, 46. doi: 10.1029/2009wr008855

Matheron, G., 1963. Principles of geostatistics. Economic Geology, 58(8): 1246-1266. doi: 10.2113/gsecongeo.58.8.1246

McBratney, A., Webster, R., 1986. Choosing functions for semi-variograms of soil properties and fitting them to sampling estimates. Eur J Soil Sci, 37(4): 617-639.

Montosi, E., Manzoni, S., Porporato, A., Montanari, A., 2012. An ecohydrological model of malaria outbreaks. Hydrol Earth Syst Sc, 16(8): 2759-2769. doi: 10.5194/hess-16-2759-2012

Njoku, E.G., Jackson, T.J., Lakshmi, V., Chan, T.K., Nghiem, S.V., 2003. Soil moisture retrieval from AMSR-E. Ieee T Geosci Remote, 41(2): 215-229. doi: 10.1109/Tgrs.2002.808243

Owe, M., Jones, E.B., Schmugge, T.J., 1982. Soil-Moisture Variation Patterns Observed in Hand County, South-Dakota. Water Resour Bull, 18(6): 949-954.

Pal, J.S., Eltahir, E.A.B., 2001. Pathways relating soil moisture conditions to future summer rainfall within a model of the land-atmosphere system. J Climate, 14(6): 1227-1242. doi: 10.1175/1520-0442(2001)014<1227:Prsmct>2.0.Co;2

Patz, J.A., Strzepek, K., Lele, S., Hedden, M., Greene, S., Noden, B., Hay, S.I., Kalkstein, L., Beier, J.C., 1998. Predicting key malaria transmission factors, biting and entomological inoculation rates, using modelled soil moisture in Kenya. Trop Med Int Health, 3(10): 818-827. doi: 10.1046/j.1365-3156.1998.00309.x

Pellenq, J., Kalma, J., Boulet, G., Saulnier, G.M., Wooldridge, S., Kerr, Y., Chehbouni, A., 2003. A disaggregation scheme for soil moisture based on topography and soil depth. J Hydrol, 276(1-4): 112-127. doi: 10.1016/S0022-1694(03)00066-0

Petrone, R.M., Price, J.S., Carey, S.K., Waddington, J.M., 2004. Statistical characterization of the spatial variability of soil moisture in a cutover peatland. Hydrol Process, 18(1): 41-52. doi: 10.1002/Hyp.1309

Phillips, A.J., Newlands, N.K., Liang, S.H.L., Ellert, B.H., 2014. Integrated sensing of soil moisture at the field-scale: Measuring, modeling and sharing for improved agricultural decision support. Comput Electron Agr, 107: 73-88. doi: 10.1016/j.compag.2014.02.011

Priestley, C.H.B., Taylor, R.J., 1972. Assessment of Surface Heat-Flux and Evaporation Using Large-Scale Parameters. Mon Weather Rev, 100(2): 81-+. doi: 10.1175/1520-0493(1972)100<0081:Otaosh>2.3.Co;2

Ranney, K.J., Niemann, J.D., Lehman, B.M., Green, T.R., Jones, A.S., 2015. A method to downscale soil moisture to fine resolutions using topographic, vegetation, and soil data. Adv Water Resour, 76: 81-96. doi: 10.1016/j.advwatres.2014.12.003

Reichle, R.H. et al., 2017. Global Assessment of the SMAP Level-4 Surface and Root-Zone Soil Moisture Product Using Assimilation Diagnostics. J Hydrometeorol, 18(12): 3217-3237.

Roth, K., Schulin, R., Flühler, H., Attinger, W., 1990. Calibration of time domain reflectometry for water content measurement using a composite dielectric approach. Water Resour Res, 26(10): 2267-2273.

Ryu, D., Famiglietti, J.S., 2005. Characterization of footprint-scale surface soil moisture variability using Gaussian and beta distribution functions during the Southern Great Plains 1997 (SGP97) hydrology experiment. Water Resour Res, 41(12). doi: 10.1029/2004wr003835

Seuffert, G., Gross, P., Simmer, C., Wood, E.F., 2002. The influence of hydrologic modeling on the predicted local weather: Two-way coupling of a mesoscale weather prediction model

and a land surface hydrologic model. J Hydrometeorol, 3(5): 505-523. doi: 10.1175/1525-7541(2002)003<0505:Tiohmo>2.0.Co;2

Shoop, S., Affleck, R., Collins, C., Larsen, G., Barna, L., Sullivan, P., 2005. Maneuver analysis methodology to predict vehicle impacts on training lands. J Terramechanics, 42(3-4): 281-303. doi: 10.1016/j.jterra.2004.10.012

Takagi, K., Lin, H.S., 2011. Temporal Dynamics of Soil Moisture Spatial Variability in the Shale Hills Critical Zone Observatory. Vadose Zone J, 10(3): 832-842. doi: 10.2136/vzj2010.0134

Vereecken, H., Kamai, T., Harter, T., Kasteel, R., Hopmans, J., Vanderborght, J., 2007. Explaining soil moisture variability as a function of mean soil moisture: A stochastic unsaturated flow perspective. Geophys Res Lett, 34(22). doi: 10.1029/2007gl031813

Vero, S.E., Antille, D.L., Lalor, S.T.J., Holden, N.M., 2014. Field evaluation of soil moisture deficit thresholds for limits to trafficability with slurry spreading equipment on grassland. Soil Use Manage, 30(1): 69-77. doi: 10.1111/sum.12093

Walker, J.P., Willgoose, G.R., Kalma, J.D., 2001. The Nerrigundah data set: Soil moisture patterns, soil characteristics, and hydrological flux measurements. Water Resour Res, 37(11): 2653-2658. doi: 10.1029/2001wr000545

Wang, Y.Q., Shao, M.A., 2013. Spatial Variability of Soil Physical Properties in a Region of the Loess Plateau of Pr China Subject to Wind and Water Erosion. Land Degrad Dev, 24(3): 296-304. doi: 10.1002/ldr.1128

Western, A.W., Bloschl, G., Grayson, R.B., 1998. Geostatistical characterisation of soil moisture patterns in the Tarrawarra a catchment. J Hydrol, 205(1-2): 20-37. doi: 10.1016/S0022-1694(97)00142-X

Western, A.W., Grayson, R.B., 1998. The Tarrawarra data set: Soil moisture patterns, soil characteristics, and hydrological flux measurements. Water Resour Res, 34(10): 2765-2768. doi: 10.1029/98wr01833

Western, A.W., Grayson, R.B., Bloschl, G., 2002. Scaling of soil moisture: A hydrologic perspective. Annu Rev Earth Pl Sc, 30: 149-180. doi: 10.1146/annurev.earth.30.091201.140434

Western, A.W., Grayson, R.B., Bloschl, G., Willgoose, G.R., McMahon, T.A., 1999. Observed spatial organization of soil moisture and its relation to terrain indices. Water Resour Res, 35(3): 797-810. doi: 10.1029/1998wr900065

Western, A.W., Zhou, S.L., Grayson, R.B., McMahon, T.A., Bloschl, G., Wilson, D.J., 2004. Spatial correlation of soil moisture in small catchments and its relationship to dominant spatial hydrological processes. J Hydrol, 286(1-4): 113-134. doi: 10.1016/j.jhydrol.2003.09.014

Wood, E.F., 1997. Effects of soil moisture aggregation on surface evaporative fluxes. J Hydrol, 190(3-4): 397-412. doi: 10.1016/S0022-1694(96)03135-6

APPENDIX

This appendix contains histograms results and a heteroscedastic analysis of the stochastic component of soil moisture. Histograms of π_{obs}, π^*, and π_d^* for dry, intermediate, and wet dates at Tarrawarra, Cache la Poudre, Nerrigundah, and Satellite Station are shown in Figure 17. The distributions of π_{obs} are centered at zero and appear to be approximately normal and symmetrical at all sites, which supports the introduction of normally distributed random variables in the generalized EMT+VS models. Both the indirect and direct models are able to approximate the histogram shapes for all three dates. The generalized models provide a better fit at Tarrawarra and Cache la Poudre than at Nerrigundah and Satellite Station, which is expected because these sites were manually calibrated.

Histograms of $\pi_{s,obs}$, π_s^*, and $\pi_{s,d}^*$ at Tarrawarra, Cache la Poudre, Nerrigundah, and Satellite Station are shown in Figure 18. The distributions of $\pi_{s,obs}$ appear to be normal and approximately symmetrical at all sites. The indirect model approximately reproduces the histogram shape of the observed stable pattern for all sites. However, π_s^* matches the histogram shape of $\pi_{s,obs}$ slightly better at Tarrawarra and Cache la Poudre. Despite using uncalibrated stochastic parameters, the indirect model still approximately reproduces the observed histogram shape at Nerrigundah and Satellite Station. The direct model does not reproduce the shape as well as the indirect model, which is because the direct model does not introduce any stable stochastic variations.

Histograms of $\pi_{u,obs}$, π_u^*, and $\pi_{u,d}^*$ for dry, intermediate, and wet dates at Tarrawarra, Cache la Poudre, Nerrigundah, and Satellite Station are shown in Figure 19. The distributions of

$\pi_{s,obs}$ appear to be normal and approximately symmetrical at all sites. The indirect model approximately reproduces the histogram shape of the observed unstable patterns at Tarrawarra and Cache la Poudre. As expected, the direct model produces a wider distribution than the observed unstable patterns to account for its narrower distribution in the stable pattern.

A heteroscedastic analysis was conducted to investigate whether the standard deviation of the stochastic component of soil moisture varies spatially. In particular, the standard deviations of π_{obs}, $\pi_{s,obs}$, and $\pi_{u,obs}$ are compared to seven catchment attributes and indices: LFI, REI, V, κ, S, elevation, and A. The analysis catchments Tarrawarra and Cache la Poudre are used in this analysis. The following procedure is the same for each catchment attribute. First, the values of π_{obs}, $\pi_{s,obs}$, $\pi_{u,obs}$, LFI, REI, V, κ, S, elevation, and A are determined for each location in a catchment. Second, the data are sorted by a given attribute in ascending order. Third, the attributes and corresponding stochastic soil-moisture values are grouped into bins, each containing 20 data points (except the final bin, which contains the remaining values). Fourth, the mean attribute value and the standard deviation of π_{obs}, $\pi_{s,obs}$, and $\pi_{u,obs}$ are calculated within each bin. Finally, the mean attribute values and the standard deviations are plotted against one another to examine the level of homogeneity.

The results for π_{obs}, $\pi_{s,obs}$, and $\pi_{u,obs}$ are shown in Figure 20. At Tarrawarra, the standard deviations of π_{obs}, $\pi_{s,obs}$, and $\pi_{u,obs}$ shows a decreasing trend with REI. However, Cache la Poudre shows an increasing trend. Similarly, the standard deviations show a slight increasing trend with V at Cache la Poudre. Finally, the standard deviations of π_{obs}, $\pi_{s,obs}$, and $\pi_{u,obs}$ show decreasing trends with S at Tarrawarra. However, no trend is noticeable at Cache la

Poudre. Thus, although there is evidence of slight heterogeneity in this figure, the results are inconsistent between sites. The attributes without any observable trends are shown in Figure 21. For each attribute presented in this figure, the standard deviation of π_{obs}, $\pi_{s,obs}$, and $\pi_{u,obs}$ remains relatively constant as the attribute values change.

This same analysis was conducted for the indirect model stochastic component π^* and the direct model stochastic component π_d^* using 2,000 realizations and taking the average standard deviation. Figure 22 compares the heterogeneity of the observed stochastic component to that of the modeled stochastic component (π^* and π_d^*). At Cache la Poudre, both generalized models reproduce the observed spatial variations in the stochastic component. However, at Tarrawarra, both model miss the dependence on REI and slope. Figure 23 shows the attributes without any observable trends. For each attribute presented in this figure, the indirect and direct models are able to approximate the relatively constant standard deviation values as the attribute values change.

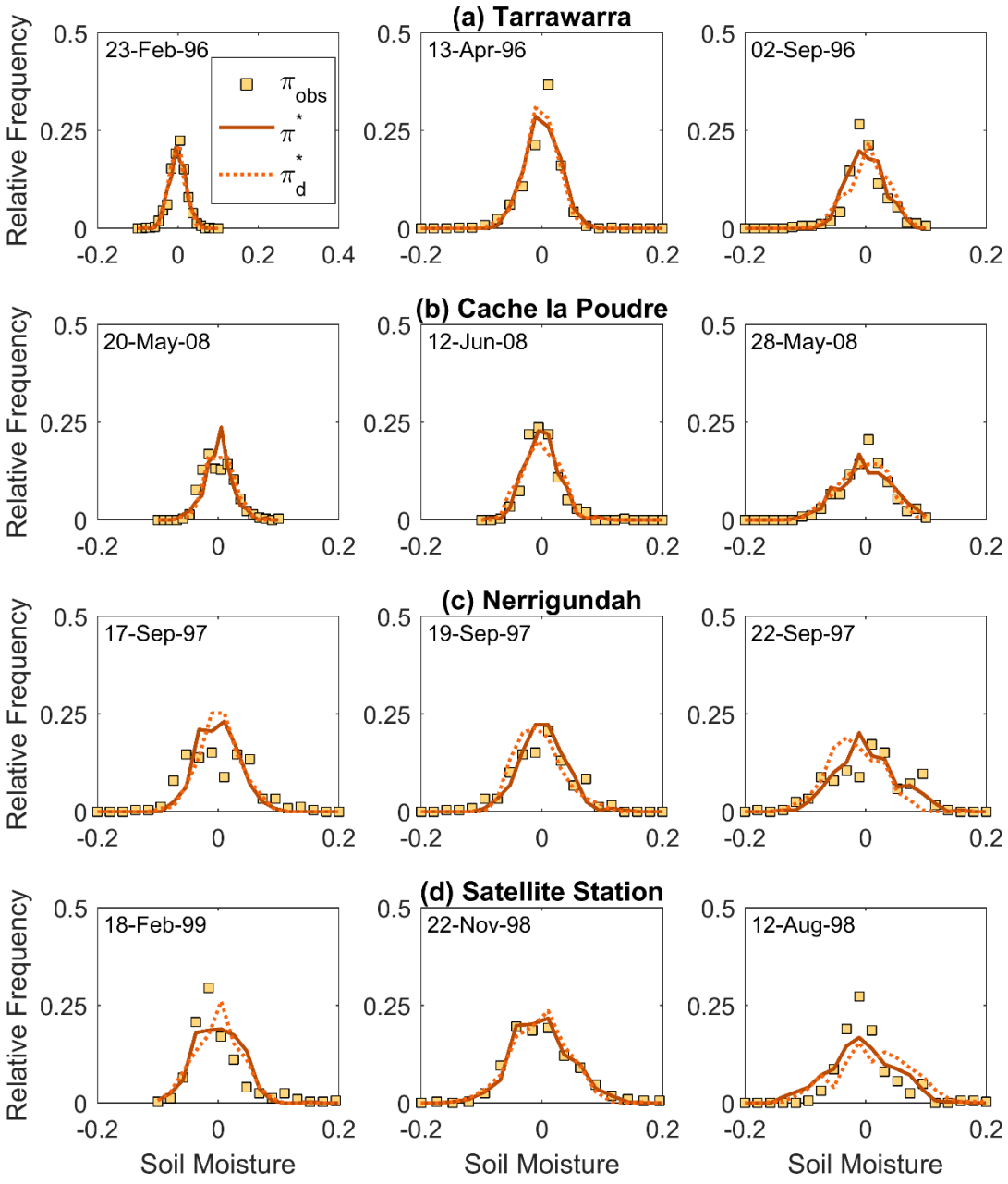

Figure 17. Example histograms of the observed stochastic component of soil moisture π_{obs}, indirect model stochastic component π^*, and direct model stochastic component π_d^* on a dry, intermediate, and wet date at (a) Tarrawarra, (b) Cache la Poudre, (c) Nerrigundah, and (d) Satellite Station.

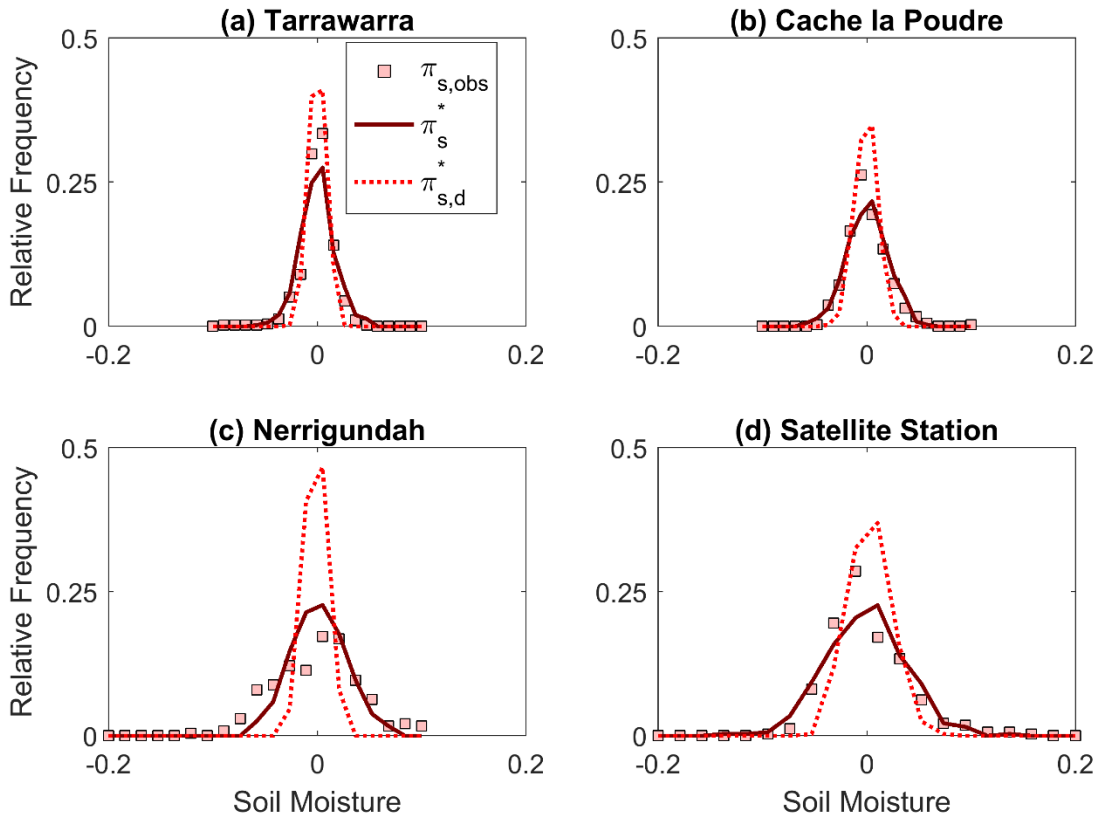

Figure 18. Example histograms of the observed stable stochastic pattern $\pi_{s,obs}$, indirect model stable pattern π_s^*, and direct model stable pattern $\pi_{s,d}^*$ at (a) Tarrawarra, (b) Cache la Poudre, (c) Nerrigundah, and (d) Satellite Station.

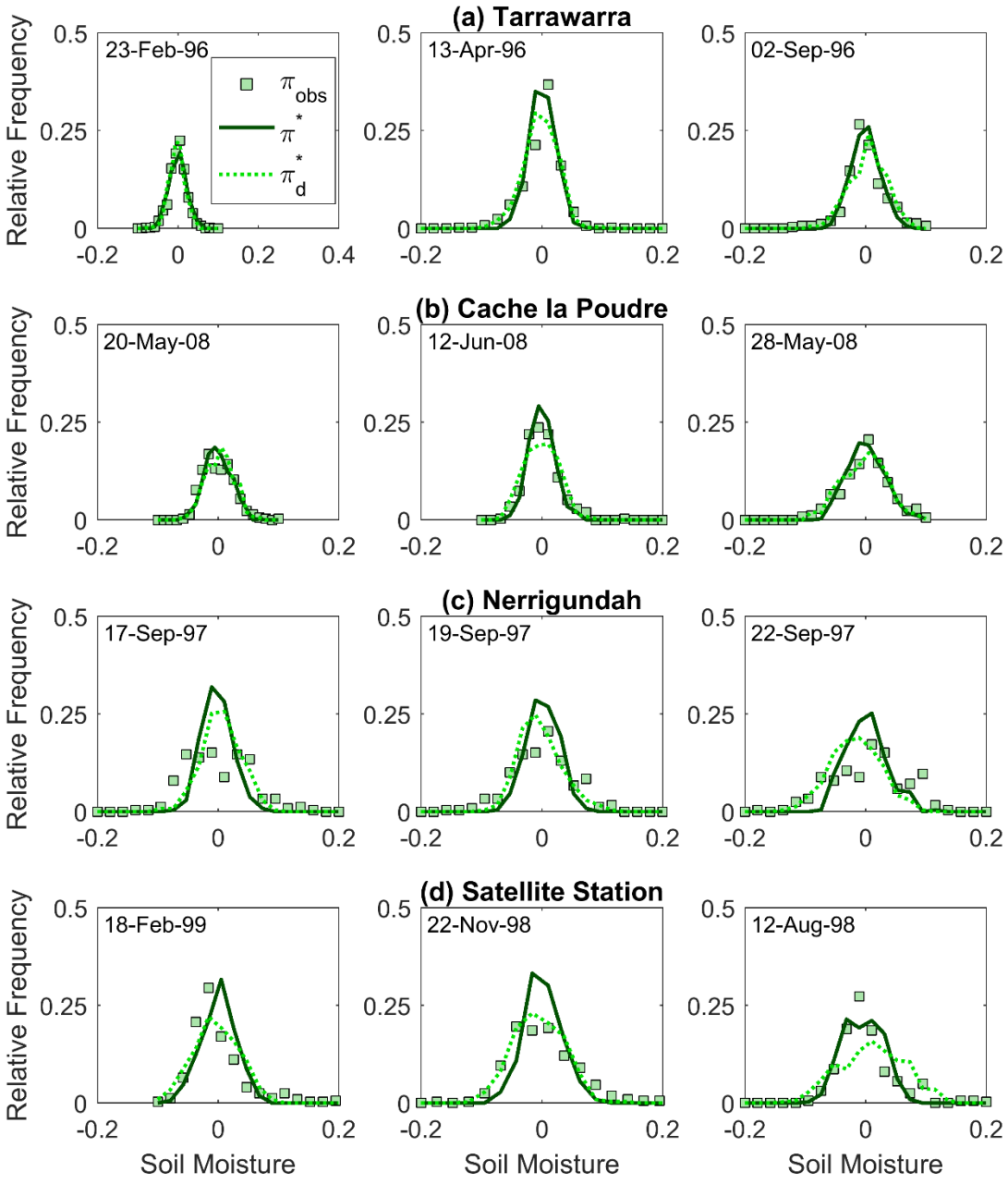

Figure 19. Example histograms of the observed unstable patterns $\pi_{u,obs}$, indirect model unstable patterns π_u^*, and direct model unstable patterns $\pi_{u,d}^*$ at (a) Tarrawarra, (b) Cache la Poudre, (c) Nerrigundah, and (d) Satellite Station.

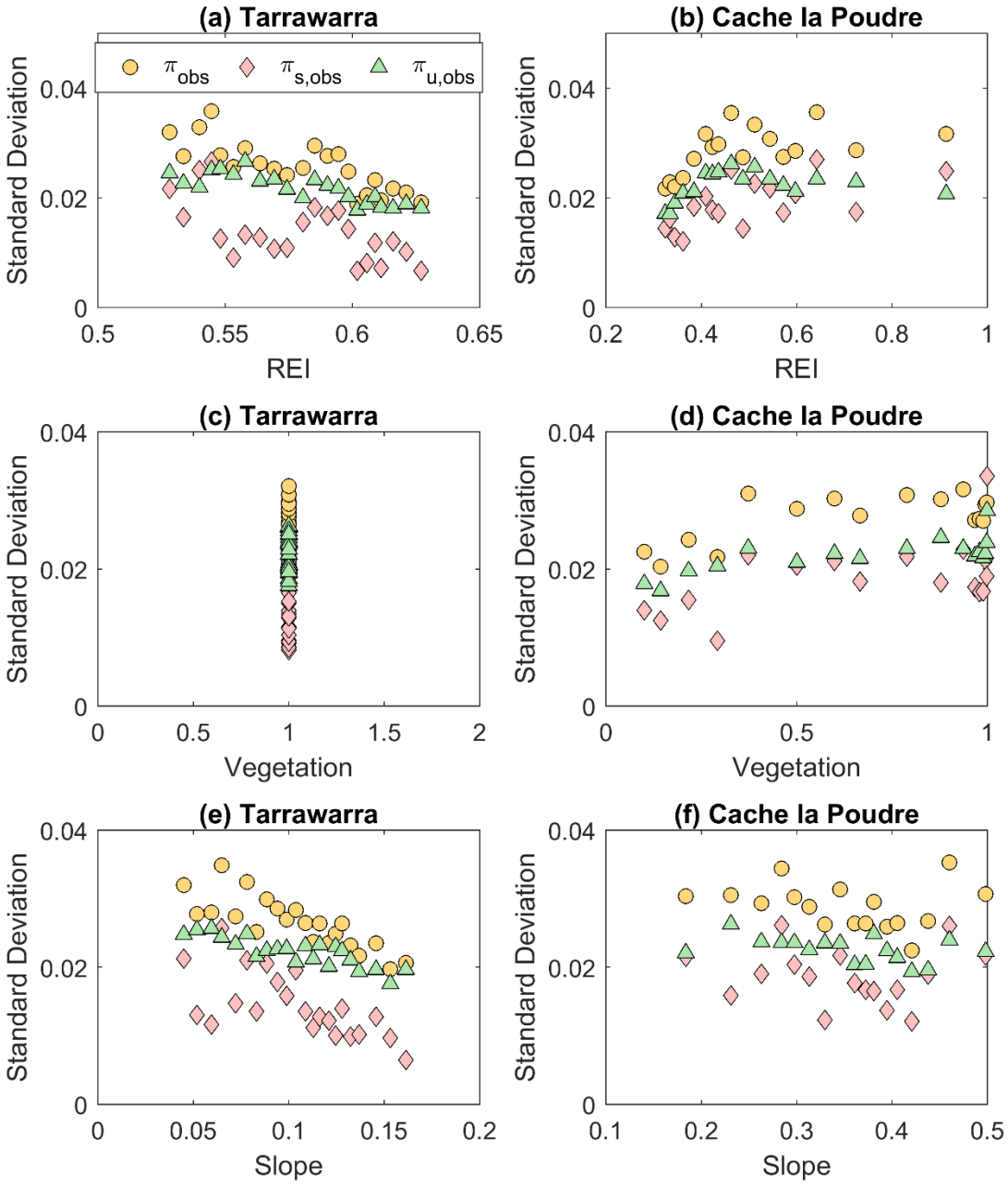

Figure 20. Comparison of standard deviation of π_{obs}, $\pi_{s,obs}$, and $\pi_{u,obs}$ to REI at (a) Tarrawarra and (b) Cache la Poudre, V at (c) Tarrawarra and (d) Cache la Poudre, and S at (e) Tarrawarra and (f) Cache la Poudre.

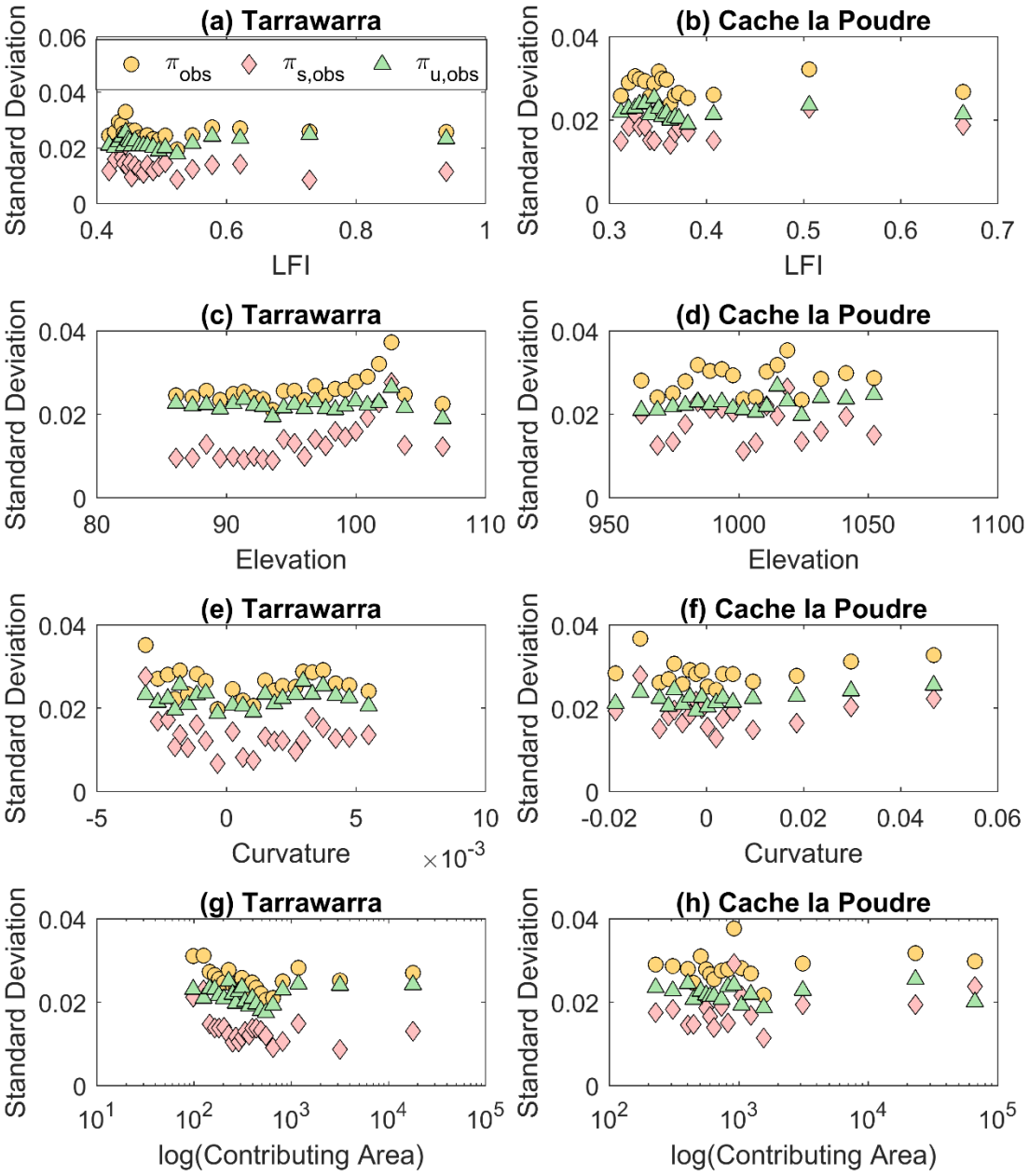

Figure 21. Comparison of standard deviation of π_{obs}, $\pi_{s,obs}$, and $\pi_{u,obs}$ to LFI at (a) Tarrawarra and (b) Cache la Poudre, elevation at (c) Tarrawarra and (d) Cache la Poudre, κ at (e) Tarrawarra and (f) Cache la Poudre, and A at (g) Tarrawarra and (h) Cache la Poudre.

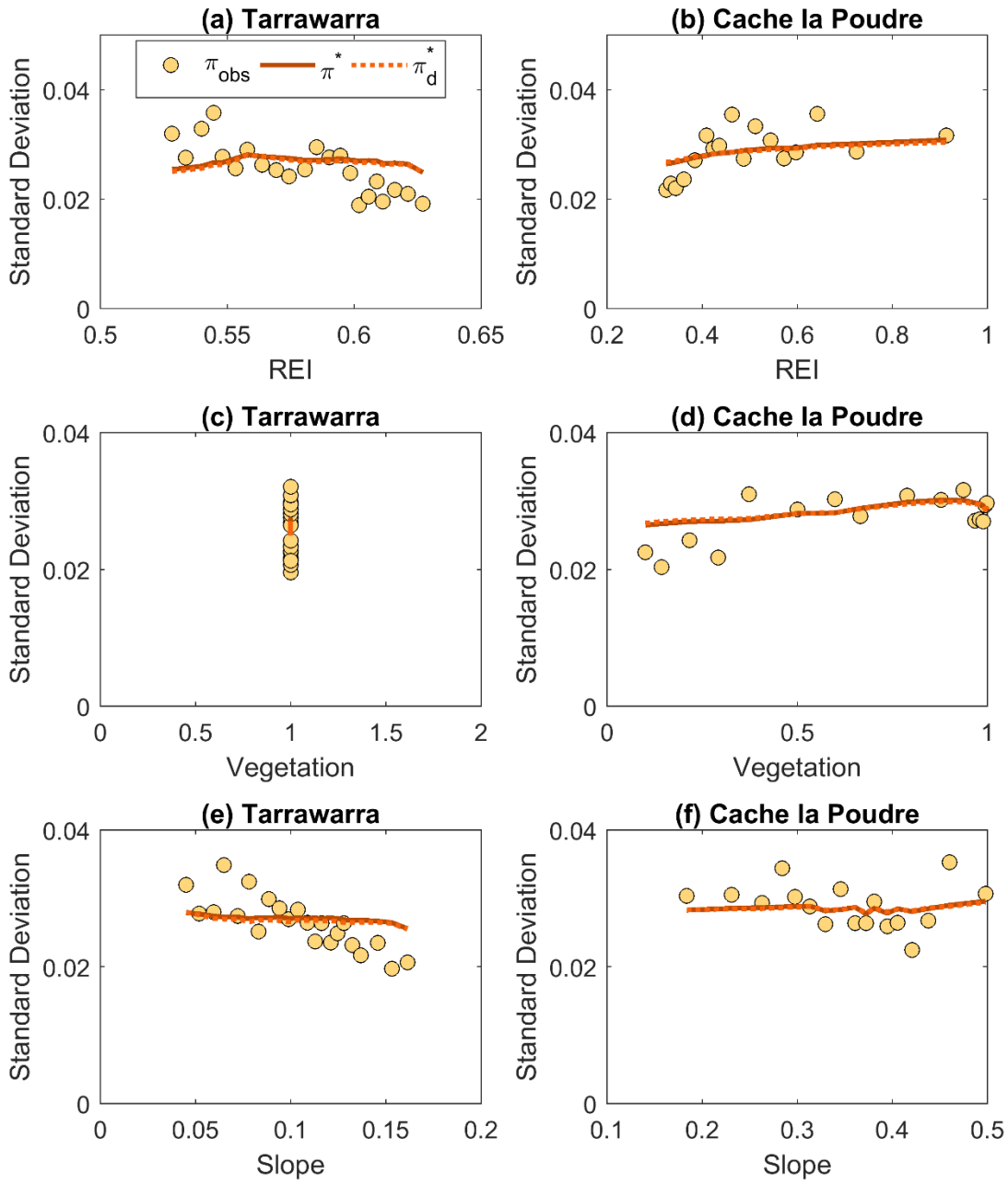

Figure 22. Comparison of standard deviation of π_{obs}, π^*, and π_d^* to REI at (a) Tarrawarra and (b) Cache la Poudre, V at (c) Tarrawarra and (d) Cache la Poudre, and S at (e) Tarrawarra and (f) Cache la Poudre.

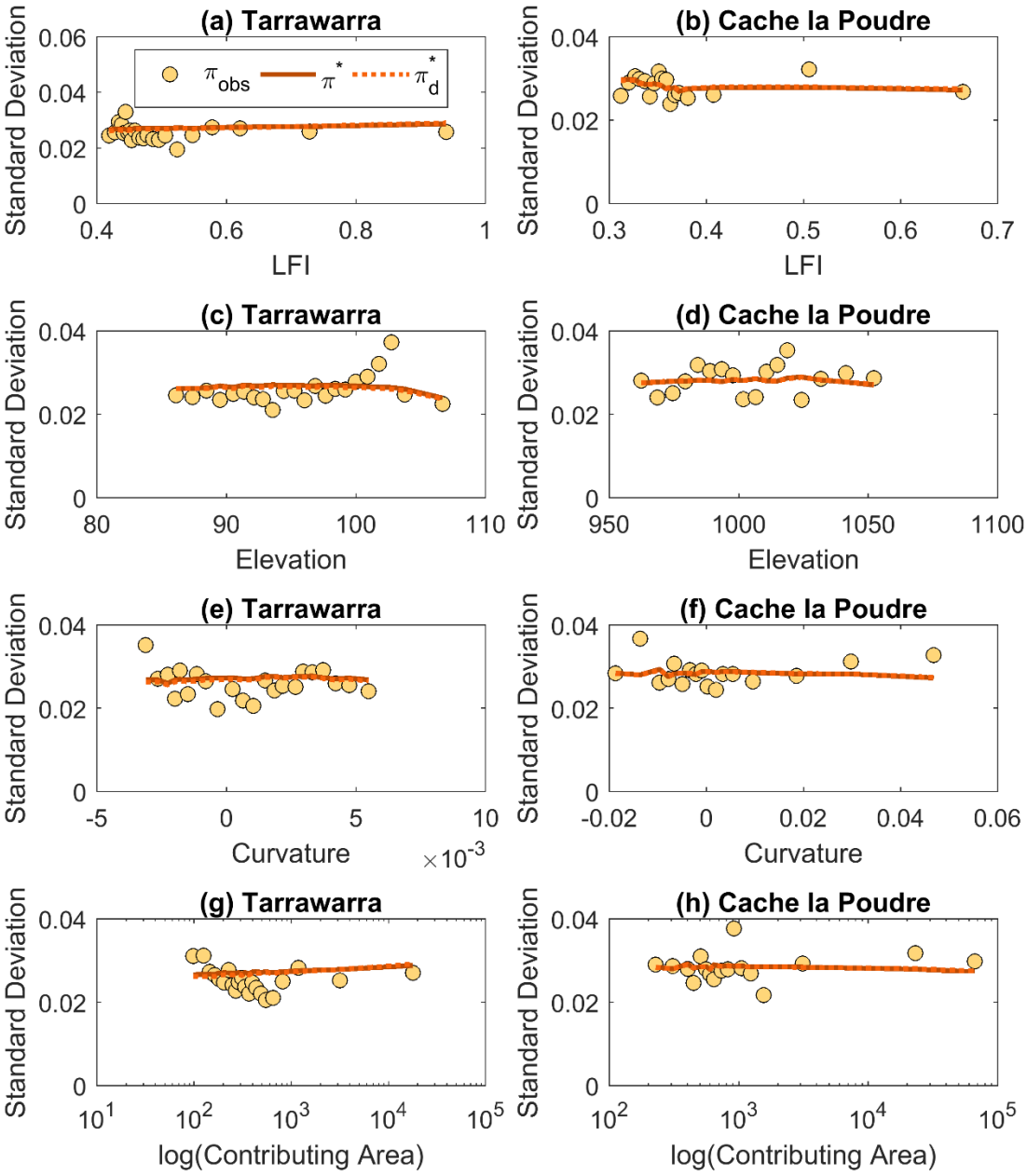

Figure 23. Comparison of standard deviation of π_{obs}, π^*, and π_d^* to LFI at (a) Tarrawarra and (b) Cache la Poudre, elevation at (c) Tarrawarra and (d) Cache la Poudre, κ at (e) Tarrawarra and (f) Cache la Poudre, and A at (g) Tarrawarra and (h) Cache la Poudre.